catalysts

MDPI

Review

Recent Progress in WS_2-Based Nanomaterials Employed for Photocatalytic Water Treatment

Aseel Yousef [1], Zeineb Thiehmed [1], Rana Abdul Shakoor [2,3] and Talal Altahtamouni [1,*]

[1] Materials Science & Technology Program, College of Arts & Sciences, Qatar University, Doha 2713, Qatar
[2] Center for Advanced Materials (CAM), Qatar University, Doha 2713, Qatar
[3] Department of Mechanical and Industrial Engineering, College of Engineering, Qatar University, Doha 2713, Qatar
* Correspondence: taltahtamouni@qu.edu.qa

Abstract: Water pollution is one of the most serious environmental issues globally due to its harmful consequences on the ecosystem and public health. Various technologies have been developed for water treatment such as photocatalysis, which has recently drawn scientists' attention. Photocatalytic techniques using semiconductors have shown an efficient removal of various water contaminants during water treatment as well as cost effectivity and low energy consumption. Tungsten disulfide (WS_2) is among the promising Transition Metal Dichalcogenides (TMDs) photocatalysts, as it has an exceptional nanostructure and special properties including high surface area and high carrier mobility. It is usually synthesized via hydrothermal technique, chemical vapor deposition (CVD), and liquid-phase exfoliation (LPE) to obtain a wide variety of nanostructures such as nanosheets and nanorods. Most common examples of water pollutants that can be removed efficiently by WS_2-based nanomaterials through semiconductor photocatalytic techniques are organic contaminants, pharmaceuticals, heavy metals, and infectious microorganisms. This review summarizes the most recent work on employing WS_2-based nanomaterials for different photocatalytic water treatment processes.

Keywords: photocatalysis; tungsten disulfide; water treatment; heterostructure; nanomaterials

Citation: Yousef, A.; Thiehmed, Z.; Abdul Shakoor, R.; Altahtamouni, T. Recent Progress in WS_2-Based Nanomaterials Employed for Photocatalytic Water Treatment. *Catalysts* **2022**, *12*, 1138. https://doi.org/10.3390/catal12101138

Academic Editors: Detlef W. Bahnemann, Ewa Kowalska, Ioannis Konstantinou, Magdalena Janus, Vincenzo Vaiano, Wonyong Choi and Zhi Jiang

Received: 9 August 2022
Accepted: 8 September 2022
Published: 28 September 2022

1. Introduction

Currently, the world is suffering from great water concerns including waterborne infections and the lack of clean water supply due to the enormous development of the industry. Today's most serious environmental aspect is water, and it is predicted to be the reason for wars in the future. Among the top priorities for the long-term economic situation are providing access to safe and valid drinking water. Chemicals such as dyes, pesticides, and pharmaceuticals as well as heavy metals and pathogenic microorganisms are among the most common pollutants that create significant threats to the natural environments and human health. This leads scientists to continuously investigate efficient water treatment technologies. Water treatment using photocatalysts can solve the problem of freshwater shortage taking place in many countries worldwide in recent decades [1–4].

Photocatalysis is the process that converts the energy of photons into chemical energy via semiconductors [5]. Photocatalytic systems have been widely used as a fascinating era in environment remediation and water cleaning, which is attributed to their effectiveness in removing contaminants [6]. The semiconductor photocatalytic technique is being studied and invested as a promising tool for water purification, as it is sustainable, has high efficiency and consumes low energy [7]. Moreover, it is considered cost-effective, environmentally friendly, and produces almost no by-products [8]. This technique implements light to degrade the pollutants into less harmful molecules [9]. Photocatalysis is considered an effective photochemical advanced oxidation process (AOP), as it is capable

of degrading contaminants in gaseous and liquid mediums, as well as killing pathogenic microorganisms by using the naturally existing solar energy as a renewable light source, which makes the process sustainable and eco-friendly [10,11]. Photocatalysis produces the hydroxyl radical (•OH) with oxidizing power of 2.80 V, which is considered relatively high [6].

Two-dimensional (2D) nanostructured materials are extensively used in water treatment for the removal of organic substances, pharmaceuticals, and heavy metal ions from water. These materials have a large surface area prepared out of layered structured materials that are strongly bonded within planes and weekly bonded between nanolayers via van der Waal forces. Generally, several approaches can be used to enhance the efficiency of photocatalytic 2D materials including doping and forming heterojunctions [12].

Recently, transition metal dichalcogenides (TMDs) are considered among the promising photocatalysts because of their tunable bandgaps, enhanced catalytic properties, ultra-thin thickness, and 2D structure [13]. Moreover, this type of nanomaterial is known for its excellent photocatalytic and electronic performances because it shows good stability, excellent carrier mobility, increased surface area, and controllable interfaces [14]. TMDs are known as 2D-layered materials in the form of (X-M-X), where M represents the transition metal sandwiched between two X, which represents the chalcogen. The thickness of each layer of TMDs is around 6–7 Å [15]. The transition-metal sulfide material is not active [16]. However, when the size is nano-scaled, the properties are significantly influenced. There is a diversity in the properties of bulk TMDs where they can be insulators such as HfS_2, semimetals such as WTe_2, metals such as NbS_2, and semiconductors such as WS_2. When these materials are exfoliated into few layers, they preserve their properties in addition to new characteristics generated by the confinement effect [17,18]. TMDs can exploit sunlight as an energy source for the removal of the bad chemicals present in water because of the significant photocatalytic potential of their nanostructure. Recent studies on TMDs show that the photocatalysts that are based on TMDs can be useful in a wider range of applications compared to other traditional photocatalysts, including TiO_2 and ZnO, which are active only under the UV light region, whereas TMDs can react to visible light as well [19].

Tungsten disulfide (WS_2) is a TMD that consists of S-W-S planes bound to each other via van der Waals interactions. The first forms of WS_2 were described in 1992 as inorganic polyhedral, cylinders, and fullerene-like (IF) nanomaterials [20]. WS_2 can be implemented in plenty of applications including photodetectors, solar cells, batteries, etc. The bandgap of the semi-conductive version ranges from 1.3 to 2.1 eV depending on the number of layers. WS_2 is a promising photocatalyst due to its direct bandgap transition, large spin-orbit coupling, and strong quantum confinement effect [21]. Exfoliating the bulk WS_2 to nanosheets can control its bandgap from indirect to direct type [22].

This review aims to highlight the recent work conducted on WS_2-based photocatalysts for water treatment through the incorporation in several treatment processes including the degradation of organic contaminants, reduction of heavy metals, decomposition of pharmaceuticals, and disinfection of microorganisms. In addition, this review introduces some techniques that are commonly employed to synthesize WS_2 in different nanostructures.

2. Background

2.1. Fundamentals of Photocatalytic Degradation of Pollutants in Water

Photocatalysis involves the acceleration of a photogenerated electron with the aid of a catalyst that is not changed or consumed during the reaction [23]. The photocatalytic reaction has a general mechanism that includes the following essential stages:

$$\text{Photocatalyst} + h\nu \text{ è photocatalyst}^*(e_{CB}^- + h_{VB}^+) \quad (1)$$

$$\text{Photocatalyst}^*(e_{CB}^- + h_{VB}^+) \text{ è photocatalyst} + h\nu \quad (2)$$

$$\text{Photocatalyst}^*(e_{CB}^- + h_{VB}^+) + A + C \text{ è photocatalyst} + A^{\bullet -} + C^{\bullet +} \quad (3)$$

Electrons in a solid material are located in an energy spectrum that is composed of the valence band (VB) and the conduction band (CB). Generally, the difference between the top of VB and the bottom of CB in a photosensitive material is called a band gap [24]. When the photosensitive material absorbs light with an energy higher than that of the band gap of the material, an electron (e^-) moves from the VB to CB leaving a hole (h^+) in the VB. In this case, the electron is mobile within the excitation zone and possesses a high reduction potential. In addition, the generated hole is mobile and acts as a one-electron oxidizer. The next stage could be one of the two options: (i) the electron moves back to the VB to regenerate the photocatalyst (Equation (2)) or (ii) redox reaction takes place between the electron-hole pair, and the molecules exist on the surface of the material (Equation (3)) [25].

Water is a necessary component for the Earth's living forms. Fresh water is causing havoc worldwide due to the drastic industrialization causing water pollution. Photocatalysis is considered one of the promising routs for wastewater treatment through the mechanism mentioned. In the case of wastewater photocatalytic treatment, electrons and holes react with O_2 and H_2O on the surface of the photocatalyst generating superoxide radical anions ($O_2^{\bullet -}$) and hydroxyl radicals ($^{\bullet}OH$), respectively, which react with the pollutants present in wastewater as shown in Equations (4)–(6) and in Figure 1 [26–28].

$$O_2 + e_{CB}^- \text{ è } O_2^{\bullet -} \quad (4)$$

$$O_2^{\bullet -} + \text{pollutants è degradation products} \quad (5)$$

$$OH + \text{pollutants è degradation products} \quad (6)$$

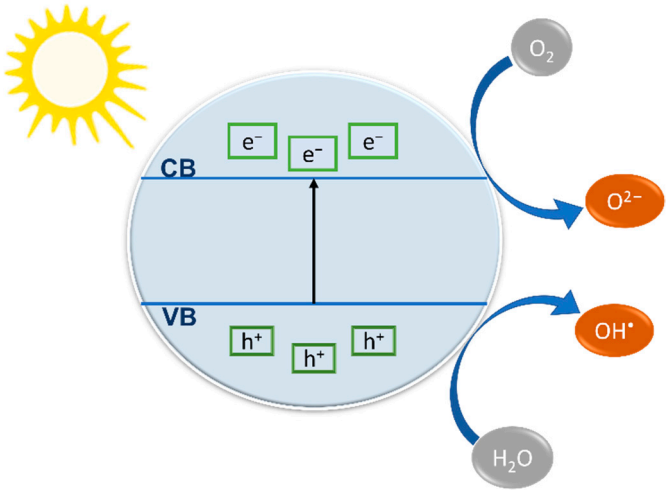

Figure 1. Schematic illustration of simplified mechanism of photocatalytic water treatment.

2.2. The Most Common Photocatalysts

Titanium dioxide (TiO_2): One of the most common photocatalysts is titanium dioxide due to its natural abundance, low cost and increased efficiency and stability. However, it has some disadvantages including a wide band gap that responds to UV light irradiation only, which causes an increased recombination rate [29,30]. Doping is an efficient method for enhancing the activity of TiO_2, where it can be doped with metals such as Ni and Pd [31].

Graphitic carbon nitride (g-C_3N_4): It is a metal-free photocatalyst that is stable and harvests light effectively with a good band gap energy of 2.7 eV. This photocatalyst is commonly used in photocatalytic reduction and oxidation of water as well as in the degradation of some pollutants. However, g-C_3N_4 showed some limitations such as the high

rate of recombination, which reduces its photocatalytic activity. Graphitic carbon nitride can be modified by constructing composites along with some semiconductors such as ZnO, in order to enhance its photocatalytic activity [32,33].

3. WS_2 As a Photocatalyst

3.1. Structure

WS_2 is found in two different phases, which are prismatic trigonal 2H phase and octahedral 1T phase, and each phase has different properties, where 2H-WS_2 is semiconducting, and 1T-WS_2 exhibits metallic properties. Both phases can be transformed into one another under certain conditions [34–36]. The bulk hexagonal WS_2 (2H-WS_2) shows an indirect band gap, whereas it exhibits an indirect-to-direct band gap transition when it is a monolayer [37,38]. The lattice parameters *a* and *c* for 2H-WS_2 are 3.155 Å and 12.349 Å, respectively, and the internal coordinate *z* that determines the interlayer sulfur plane distance for bulk 2H-WS_2 is 1.573 Å [39,40].

3.2. Properties

Among the 2D materials, WS_2 is more abundant in the crust of Earth, has less toxicity, and is cheaper compared to other TMDs. Moreover, it is special for its extraordinary properties including high surface area, favorable electrochemical activity, photocatalytic and electronic efficiency, high carrier mobility, biocompatibility, and its tunable bandgap. In addition, WS_2 is commonly used as a light-absorbing material due to its broad absorption spectrum, which makes it an efficient photocatalytic material. However, WS_2 shows some limitations for some photocatalytic applications, as the band edge potential of its conduction band minimum does not match the potential requirements for photocatalytic water splitting for instance [41]. WS_2 can show a low indirect band gap (less than 1.5 eV) and a higher direct bandgap (larger than 2 eV) depending on the synthesis technique used [42–44]. This relatively narrow band gap increases the light absorption region to 910 nm, which enables it to undergo the redox chemistry required for degradation of organic pollutants [45].

3.3. Synthesis

Various methods have been employed for the WS_2 synthesis, among them are the mechanical activation method, sol-gel method, thermal evaporation technique, liquid-phase exfoliation method, hydrothermal method, and chemical deposition techniques. In addition, WS_2 can be synthesized with a wide range of morphologies including nanosheets, nanofibers, and nanorods [20].

The hydrothermal route is among the promising techniques, as it is a simple process, yields a highly pure product, and is environmentally friendly. Cao, Liu, Hussain, and others succeeded in synthesizing different nanostructures of WS_2 with various morphologies including nanorods, nanofibers, nanoparticles, and nanosheets via a hydrothermal route with the addition of the surfactants polyethylene glycol (PEG) and cetyltrimethylammonium ammonium bromide (CTAB). The surfactants were found to affect the fabrication of different morphologies of WS_2 nanostructures [46].

In addition, a simple hydrothermal method was used to synthesize hexagonal WS_2 platelets with a thickness of ~20 to 100 nm and exhibited a photocatalytic activity against rhodamine B (RhB) dye under visible light irradiation [47]. Table 1 states some of the most recent examples of WS_2 nanostructured synthesized hydrothermally and used for different photocatalytic water treatments.

Table 1. Most recent examples of hydrothermal-synthesized WS_2 nanostructures employed for different applications.

Precursors	Conditions	Morphology	Application	Ref.
Sodium tungstate, thiourea, hydroxylamine hydrochloride	Autoclave, 60 °C for 8 h	Nanosheets	Photocatalytic degradation of antibiotic nitrofurantoin (NFT)	[44]
Sodium tungstate, thioacetamide, oxalic acid.	Autoclave, 200 °C for 24 h.	Nanoflakes	Photodegradation of methylene blue	[48]
Sodium tungstate, thiourea, hydroxylamine hydrochloride, CTAB, hydrochloric acid.	Autoclave, 180 °C for 24 h.	Nanosheets	Hydrogen evolution	[49]
Sodium tungstate, L-cysteine.	Autoclave, 180 °C for 24 h.	Nanosheets	Biomedical evaluation	[50]

Chemical vapor deposition (CVD) is known as one of the most powerful methods to obtain large area growth of thin 2D TMDs. It involves the growth of the 2D TMD material by the co-evaporation of the metal oxide (tungsten oxide WO_x) and the chalcogen source (sulfur), and then, a stable nanostructure will be formed over a proper substrate. This synthesis process depends on the type of the substrate, the temperature, and atomic gas flux [51,52]. The CVD method has shown a highly reliable production of large area WS_2 compared to the exfoliation method, which lacks film uniformity [15]. Table 2 shows several examples of the most recent work on the synthesis of WS_2 nanostructures using CVD.

Table 2. Most recent examples of WS_2 nanostructures synthesized by CVD.

Precursors	Conditions	Substrate	Morphology	Ref.
WO_3 and sulfur	Ar + H_2 (95% + 5%) environment at 100 SCCM, 850 °C for WO_3 and 220 °C for sulfur 10 min	c-plane sapphire	Monolayer thin film	[53]
WO_3 and sulfur	Ar 75 SCCM, 250 °C for S, and 920 °C for 15 min	Si/SiO	Bilayer ribbons	[54]
WO_3 and sulfur	Ar + H_2 (95% + 5%) 50 SCCM, 850°C for 10 min	SiO_2/Si	Nanorods	[55]
WO_3 and sulfur	Ar 150 SCCM, 880 °C for 15 min	SiO_2/Si with Au foil on the center	2D film	[56]

Liquid phase exfoliation (LPE) is one of the versatile methods for producing high yield 2D nanosheets of a wide range of materials including WS_2 [57,58]. LPE is known as a two-step process that delaminates van der Waals crystals mechanically in a liquid medium. To prevent the interactions among the layers, a high-energy process is employed such as sonication. After that, colloidal stabilization via proper solvents or surfactants takes place to overcome reaggregation. Further casting or printing can be applied to the produced nanosheets to obtain thin films for a wide range of applications including nanocomposites and optoelectronic devices [59–62]. Table 3 presents some examples of recent work on the synthesis of WS_2 nanosheets by LPE.

Table 3. Recent examples of LPE-fabricated WS_2 nanosheets.

Processing	Solvent	Ref.
Sonication for 3 h. Centrifugation at 3000 rpm for 20 min.	N-Methyl-2-pyrrolidone (NMP)	[63]
Oxygen plasma treatment followed by Sonication at 400 W.	Dimethyl sulfoxide (DMSO) and water	[64]
Sonication for 5 days. Centrifugation in 3500 rpm for 60 min.	35 vol% ethanol @ water	[65]
Ultrasonication for 6 h in a water bath.	N-Methyl-2-pyrrolidone (NMP)	[66]

4. Photocatalytic Water Treatment Using WS_2 and Heterostructures

When different semiconductors having different energy gaps are coupled to form heterostructures, this will result in controlling the recombination process of the photogenerated charge carriers, improving the photocatalytic activity, reducing the bandgap, and moving the optical response to be in the visible light region to enable the investment of the solar energy. Forming a well-matched conduction band and valence band levels leads to a dimensional separation between the photogenerated electrons and holes [67]. The construction of heterojunctions is among the most common methods for photocatalysts fabrication and modification because it provides high activity and visible light response [68]. When using WS_2 as a cocatalyst, semiconductor–semiconductor, or metal-semiconductor, heterojunctions will be constructed, which will result in creating more interfaces [69]. As a result, the charge separation and migration can be improved, and hence, the photoactivity will be enhanced [70].

4.1. Photocatalytic Degradation of Organic Substances

Enormous quantities of organic pollutants such as synthetic dyes, fertilizers, solvents, and pesticides are being released into the environment and the aquatic ecosystem, which can cause serious environmental problems [1]. These organic compounds are mostly stable and do not undergo biodegradation or photodegradation naturally and hence cause harm to humans and animals in both the short and long term [71]. In addition, organic pollutants can harm human health by causing cancers and mutations, nausea, mental confusion, and Alzheimer's. Thereby, searching for new technologies for the removal of organic pollutants is demanded. This is because the traditional techniques showed some restrictions and limitations such as unaffordable operation costs, poor removal efficiency, complicated processes, and low adaption to many organic structures [72,73]. AOPs can be used to eliminate organic pollutants from wastewater via direct and indirect processes where hydroxyl radicals are employed to hydroxylate or dehydrogenate the pollutants, and then, they will finally mineralize [74,75]. Therefore, the main advantage of using AOP for the degradation of organic pollutants is the complete destruction it guarantees instead of changing them into another phase, and without the need for toxic oxidants such as chlorination [76]. Photocatalysis can be utilized for degrading organic pollutants, as it provides good reproducibility, simplicity, high efficiency, and low cost. Photocatalysis can degrade organic pollutants into harmless products. The photocatalysis process is mainly a reaction between the organic pollutants and oxidizing and reducing agents, which are holes and electrons generated under UV or visible light irradiation on the photocatalyst's surface [68].

4.1.1. Photocatalytic Degradation of Organic Substance Using WS_2 Nanostructures

Mishra, Lakshmi, and Huang invented an eco-friendly method for synthesizing few-layer WS_2 nanosheets using a dilute aqueous solution of household detergent instead of sophisticated surfactants for the exfoliation process, which lowers the cost and the environmental hazards. SEM image of the synthesized WS_2 nanosheets is shown in Figure 2a. Fortunately, the method produced WS_2 nanosheets of thermal stability, Raman spectra, and optical absorption that are similar to other synthesis techniques. More importantly,

the synthesized nanosheets exhibited efficient photocatalytic activity on the photodegradation of Brilliant Green (BG) dye in an aqueous solution under visible light irradiation. The effect of the prepared WS_2 on the concentration of BG solution is shown in Figure 2b.

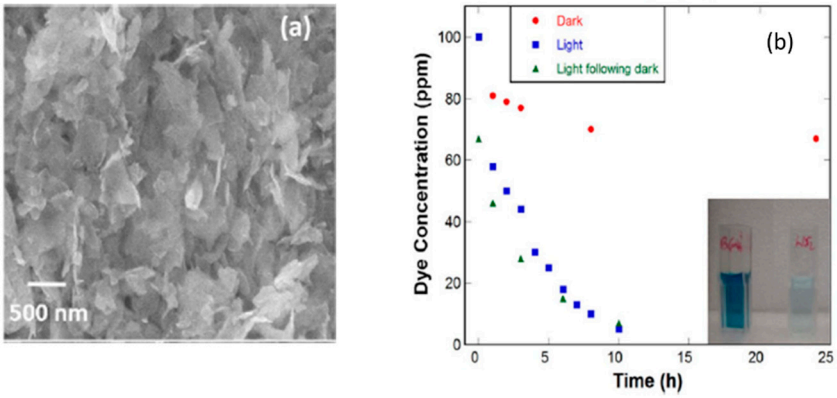

Figure 2. SEM image of the fabricated WS_2 nanosheets (**a**). Photocatalytic activity of WS_2 nanosheets: concentration change of BG solution in the presence of WS_2 (inset image represents the corresponding samples) (**b**). Reproduced with permission [19]. Copyright 2015, Springer Nature.

In addition, Hazarika and Mohanta reported a hydrothermal method for the synthesis of inorganic fullerene (IF)-type WS_2 nanoparticles and their application in the photodegradation of malachite green (MG) considering both UV and visible light. IF-WS_2 nanoparticles' morphology was observed by SEM as shown in Figure 3a,b. In addition, the band gap of the prepared WS_2 was predicted via Tauc's plot to be around 1.9 eV. The synthesized IF WS_2 nanocatalyst exhibited an enhanced photocatalytic response with the dye degradation that reached 71.2%. The photodegradation activity of the as-prepared nanoparticles was studied as shown in Figure 3c,d.

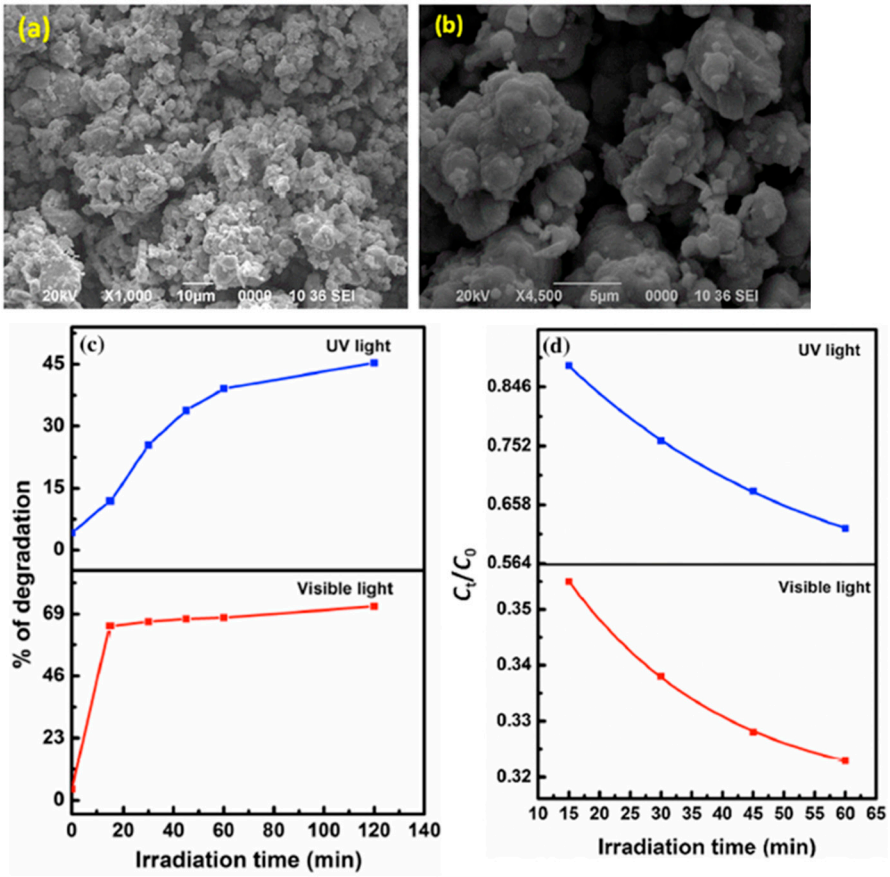

Figure 3. SEM images of the prepared WS_2: low magnification (**a**), high magnification (**b**), the degradation percentage (**c**), pseudo-first-order plots (**d**) under the mentioned conditions on a comparative basis. Reproduced with permission [22]. Copyright 2017, Springer Nature.

Another successful work by Vattikuti and his team was the synthesis of hexagonal-shaped WS_2 platelets via the simple hydrothermal method, which showed great photocatalytic activity for the photodegradation of rhodamine B (RhB) compared to the irregular WS_2 platelets. They formed the hexagonal WS_2 by the oriented attachment (OA)-self-assembly (SA) with a thickness ranging between 20 and 100 nm. SEM images of both hexagonal and irregular-shaped platelets are shown in Figure 4a,b. The synthesized platelets are kinetically stable due to their anisotropic structures and the wide surface energy distribution, as well as the predominantly open reactive sites. The optimal conditions for the growth of the platelets were 150 °C and 12h. SEM image of the corresponding sample is shown in Figure 4b. Moreover, these platelets provided a higher RhB degradation activity of 98% in 105 min, and they showed better activity than the irregular-shaped platelets according to Figure 4c.

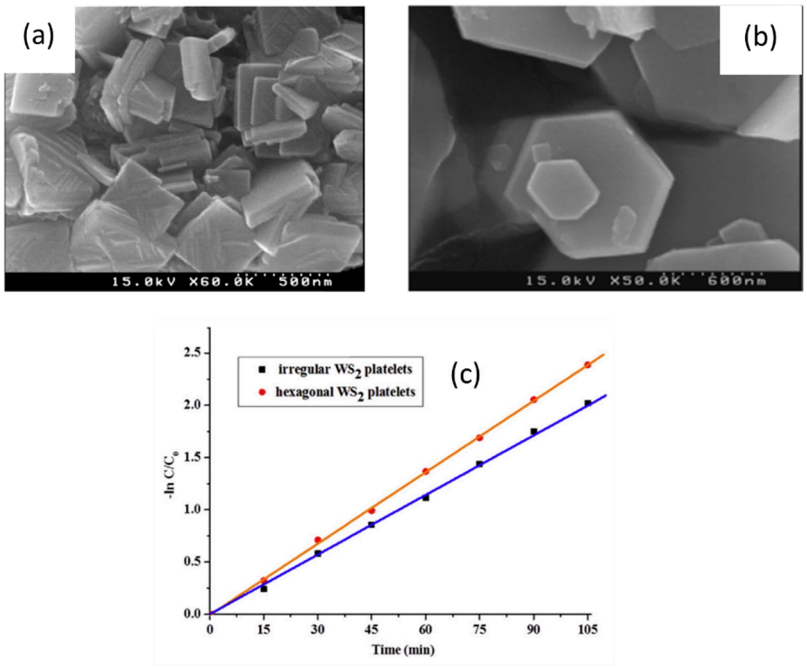

Figure 4. SEM images of as-prepared irregular WS_2 platelets (**a**) and hexagonal WS_2 platelets at optimal conditions: 150 °C, 12 h (**b**), photocatalytic degradation of RhB in the presence of irregular and hexagonal WS_2 platelets under visible light irradiation (**c**). Reproduced with permission [47]. Copyright 2016, Elsevier.

Moreover, the role of morphology and defects of WS_2 nanostructures were studied by Ashraf, Fatima, Srivastava, and Khanuja by firstly synthesizing WS_2 nanosheets (WNS) and nanorods (WNR) using the facile hydrothermal technique illustrated in Figure 5a. Both nanostructures were characterized via FE-SEM as shown in Figure 5b,c in addition to other techniques such as XRD. The photocatalytic degradation activity of each nanostructure was investigated on methylene blue (MB) and 4-chlorophenol (4-CP). Moreover, a comparative high performance liquid chromatography (HPLC) study was conducted to investigate the intermediate degradation products of 4-CP. It was concluded that nanorods showed superior photocatalytic performance over nanosheets, which could be due to the enhanced pore size and reduced defect density. Figure 5d,e shows plots that confirm the conclusion.

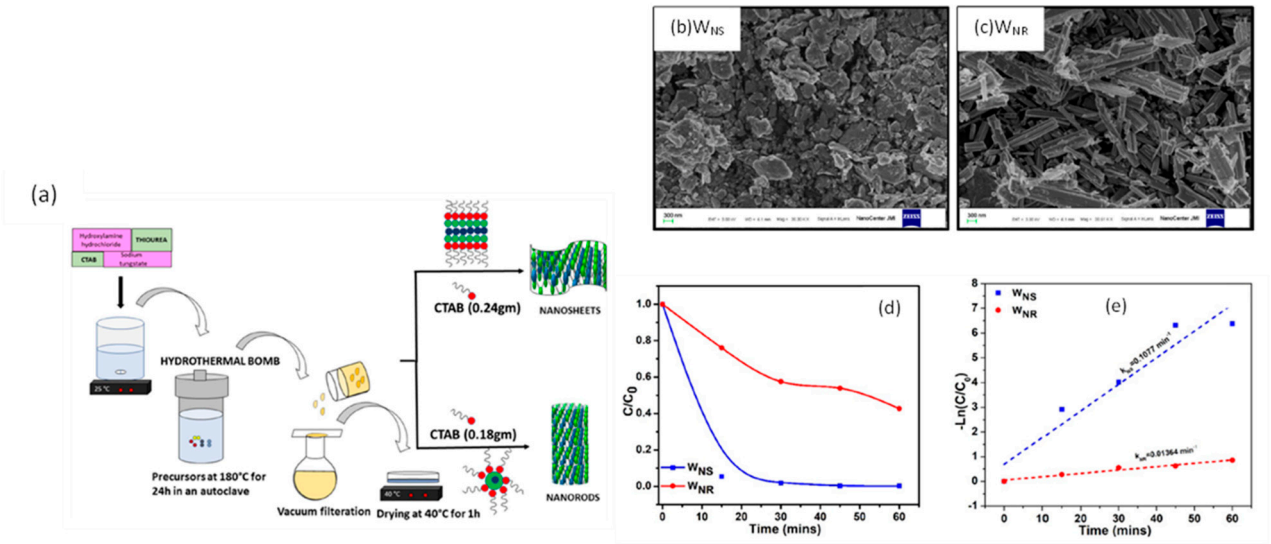

Figure 5. Schematic illustration of the synthesis of WS_2 nanostructures hydrothermally (**a**), FE-SEM images of W_{NS} (**b**) and W_{NR} (**c**), C/C_0 vs. time plot (**d**), and $-\ln(C/C_0)$ vs. time plot (**e**). Reproduced with permission [77]. Copyright 2019, Springer Nature.

Furthermore, Koyyada, Vattikuti, Shome, and others succeeded in synthesizing exfoliated hexagonal WS_2 (e-h-WS_2) platelets via the LPE process starting from hydrothermally synthesized hexagonal WS_2 (h-WS_2) platelets in DMF solvent. Figure 6a,b shows the SEM images of the fabricated h-WS_2 and e-h-WS_2, respectively. They studied the photocatalytic activity of each one and made a comparison between them in terms of the photodegradation of several organic dyes such as methyl orange (MO), Congo red (CR), rhodamine B (RhB), and phenol red (PR) under simulated solar light. Figure 6c shows the UV–Vis absorption spectra of MO against the e-h-WS_2 photocatalyst. The study showed an enhancement in the photocatalytic activity of e-h-WS_2 compared to h-WS_2, which could be due to that e-h-WS_2 exhibits a narrower band gap, higher specific surface area and more active sites than that of h-WS_2, and that was confirmed by the Brunauer–Emmett–Teller (BET) analysis, UV–Vis analysis, impedance spectroscopy, and photocurrent analysis, which is shown in Figure 6d.

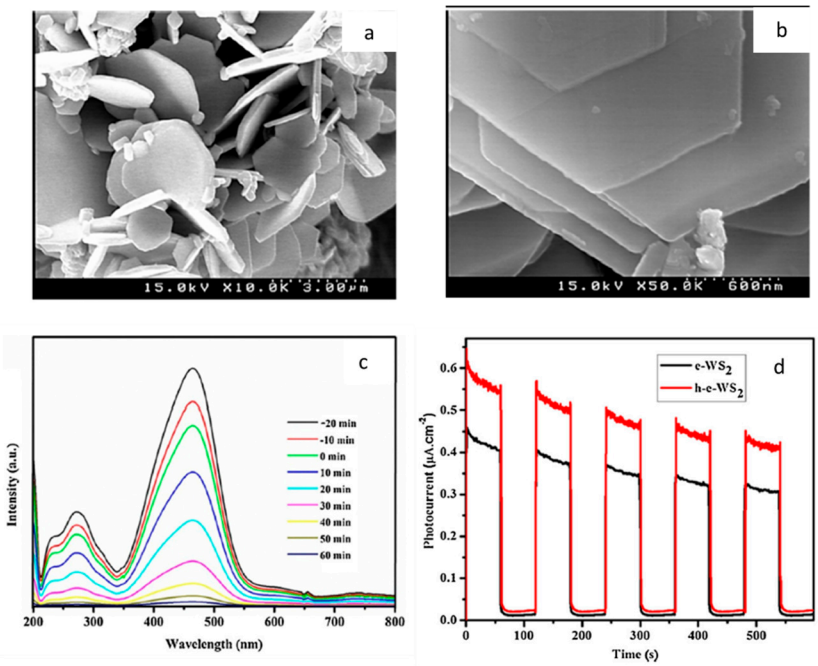

Figure 6. SEM images of h-WS_2 nanosheets (**a**), e-h-WS_2 (**b**), UV–Vis absorption spectra of MO against e-h-WS_2 photocatalyst (**c**), photocurrent response for h-WS_2 and e-h-WS_2 photocatalysts as working electrode (**d**). Reproduced with permission [78]. Copyright 2019, Elsevier.

4.1.2. Photocatalytic Degradation of Organic Substance Using WS_2 Heterostructure

WS_2/Ag

Wu, Cheng, Han, and others constructed a two-dimensional Ag/WS_2 hybrid membrane via in situ self-reduction of $AgNO_3$ on WS_2 nanoflakes. The membranes were prepared on Nylon substrates by vacuum filtration and were characterized via several methods among which is TEM as shown in Figure 7a,b. It was found that Ag nanoparticles helped in increasing the thickness and interlayer spacing of WS_2 membrane, and the photodegradation mechanism is illustrated in Figure 7c. In addition, those nanoparticles improved the photodegradation performance of the membrane by collecting photoinduced electrons from the conduction band of WS_2 to prevent recombination of the electrons and holes. The membrane produced has an outstanding UV-driven self-cleaning ability by photodegradation of dye molecules (Evans blue) in water.

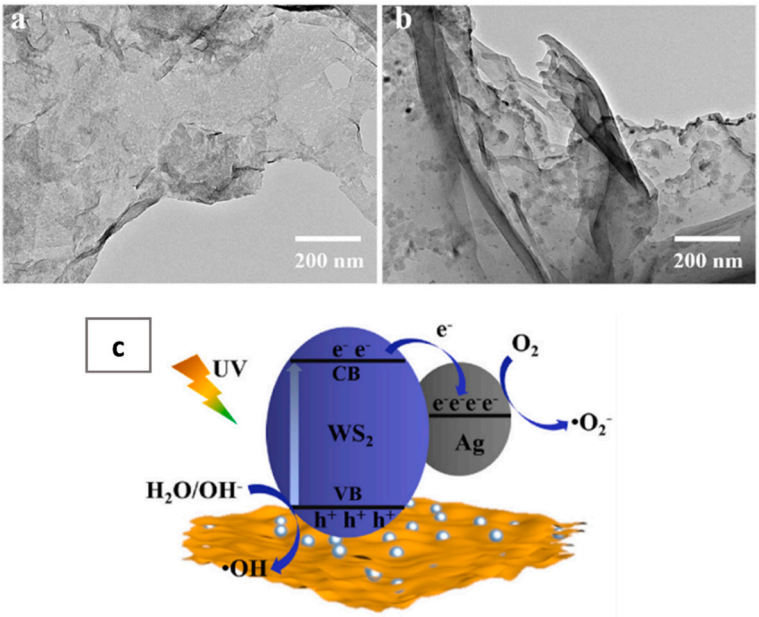

Figure 7. TEM images of hybrid Ag/WS_2 nanoflakes (**a**,**b**), schematic diagram for the photodegradation mechanism of Ag/WS_2-2 (**c**). Reproduced with permission [79]. Copyright 2022, Elsevier.

AgI/WS_2

Wu, Li, Zhang, and others synthesized an AgI/WS_2 composite by in situ growth of AgI on WS_2 nanosheets. The morphology of the fabricated AgI, WS_2 nanosheets, and the composite were analyzed using TEM as shown in Figure 8a–c. They evaluated the photocatalytic activity of the samples by photodegrading rhodamine B solution under visible light irradiation by measuring the photocatalytic degradation efficiency against RhB dye solution (Figure 8d), as well as the cycling experiments as shown in Figure 8e. It was concluded that WS_2 nanosheets enhance light absorption, recyclability, and photocatalytic activity of the pure AgI in visible and infrared light. In addition, the degradation efficiency increased with increasing the amount of WS_2 nanosheets. There is no doubt that this study contributed effectively to the application of full-spectrum-responsive photocatalysis employed for green energy production.

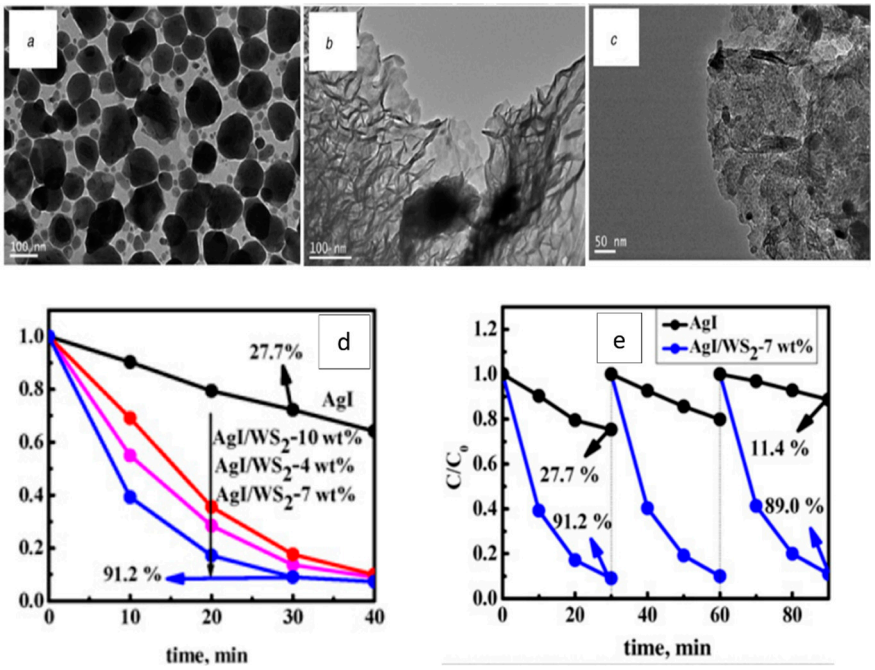

Figure 8. TEM images of AgI (**a**), WS_2 (**b**), AgI/WS_2- 7 wt hybrids (**c**), photocatalytic degradation efficiency of the prepared samples of RhB (10 mg/L) under visible light (**d**), cycling experiments of the samples for RhB photodegradation (**e**). Reproduced with permission [80]. Copyright 2019, John Wiley and Sons.

$WS_2/Bi_2O_2CO_3$

A novel flower-like $WS_2/Bi_2O_2CO_3$ photocatalyst was fabricated by Li and his team using a one-pot hydrothermal method. They synthesized the photocatalyst with a varied mass ratio of WS_2 as the following: 1, 2, 4, and 6 wt%, and then labeled them as WS_2-BOC-1, WS_2-BOC-2, WS_2-BOC-3, and WS_2-BOC-4, respectively. The team studied the morphology of the composites by FE-SEM. The composite WS_2-BOC-3 showed the best photocatalytic performance among other BOC samples and bare WS_2 as represented in Figure 9b. The morphology of WS_2-BOC-3 is represented in the FE-SEM image in Figure 9a. This heterostructure showed efficient removal of Lanasol red 5B (LR5B) with a rate constant of 1.85 times higher than $Bi_2O_2CO_3$ under UV and 3.23 times under simulated solar irradiation as shown in Figure 9c. This enhanced activity was attributed to the synergistic effect of the photoinduced charge carrier separation and transfer, the improved light harvesting ability, and the higher specific surface area resulting from the unique flower-like structure. Furthermore, the material was found to be stable and recyclable by applying cyclic testing.

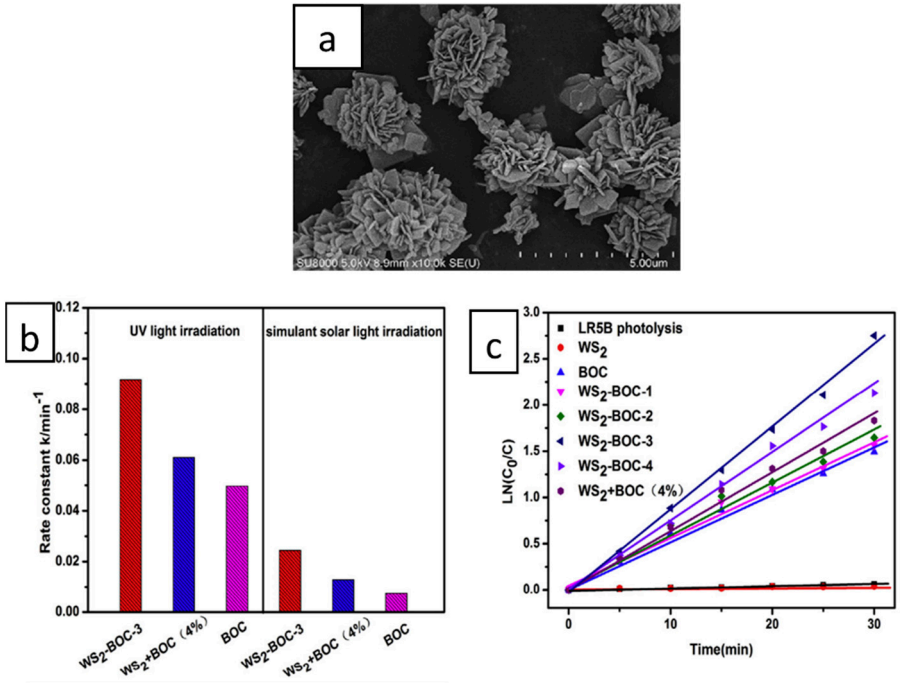

Figure 9. FE-SEM image of WS_2-BOC-3 (**a**), the rate constants for LR5B degradation under both UV and simulated solar light (**b**), the kinetic fit for LR5B degradation using the samples under UV irradiation (**c**). Reproduced with permission [81]. Copyright 2019, Elsevier.

WS_2/BiOBr

A novel heterostructured photocatalyst WS_2/BiOBr was fabricated by Fu and his team, using the facile hydrothermal method. TEM technique was used to characterize the synthesized composite as shown in Figure 10a. The fabricated quantum dots showed excellent removal efficiency toward Rhodamine B reaching a 95% of removal rate, in addition to other water pollutants such as ciprofloxacin as represented by Figure 10b. This activity is attributed to the oxygen vacancies offered by this heterostructure, which contribute to harvesting the visible light as well as the separation of photo-induced electron-hole pairs. In addition, the synergistic effect between the fabricated photocatalyst and the oxygen vacancies was found to enhance the photocatalytic process. The researchers proposed the photocatalytic mechanism via the electron spin resonance and the trapping experiment (i.e., performed to study the roles of active species in the process of CIP degradation) and proved that holes, $O_2^{\bullet-}$ and $^{\bullet}OH$ played an important role in the process.

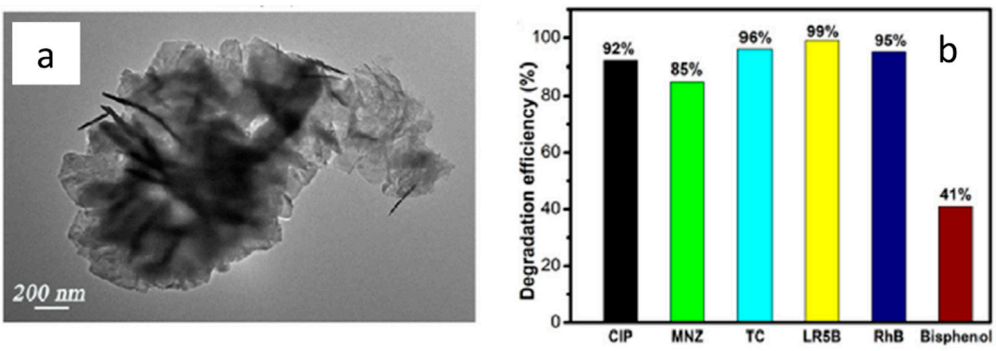

Figure 10. TEM image of WS_2/BiOBr (**a**), degradation efficiency of different pollutants with WS_2/BiOBr (**b**). Reproduced with permission [82]. Copyright 2020, Elsevier.

BiOCl/WS_2

Ashraf, Bansal, Singh, and others have reported an enhanced visible-light-driven photocatalytic response of novel 2D/2D BiOCl/WS_2 hybrid nanosheet heterojunctions ranging from 0–5% of WS_2 content. They prepared these heterojunctions by a low-cost simple solution-based sonochemical technique. They also conducted a comparative study between BiOCl and BiOCl/WS_2 hybrid nanosheet in terms of photocatalytic activity by studying their photodegradation of Malachite Green (MG) under visible light irradiation. The hybrid nanosheets (2%) (BW_2) achieved more than 99% of MG photodegradation in 60 min of irradiation. Figure 11a shows an FE-SEM image for the BW_2 nanosheet. Furthermore, the fabricated photocatalyst exhibited the highest external quantum efficiency (EQE) under UV and visible light irradiations, which was measured by the incident photon to electron conversion efficiency (IPCE). The authors highlighted the key factors in the enhancement of the photocatalytic performance of the fabricated hybrid nanosheets, which are large separation time of photogenerated charge carriers, high rate of charge transfer, high absorption of the visible range, and large IPCE values (Figure 11b) in the whole UV–Visible region. The primary active species in the photocatalytic process are found to be the OH radicals formed by the photogenerated holes on WS_2 nanosheets.

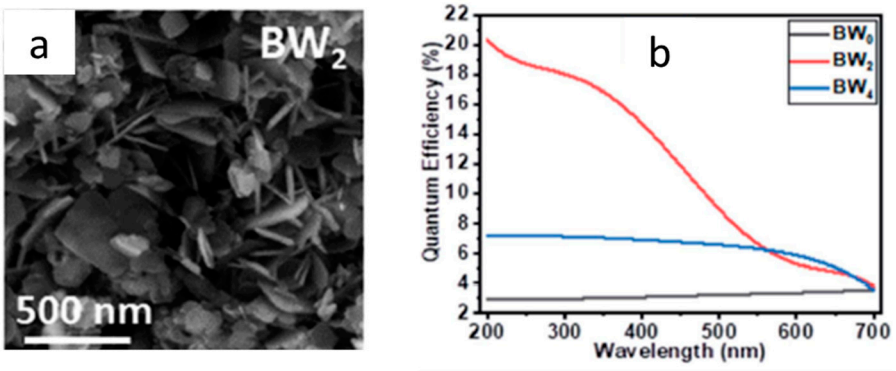

Figure 11. FE-SEM image of BW_2 hybrid nanosheet (**a**), IPCE spectra of the hybrid nanosheets BW_0, BW_2, and BW_4 measured at 0 V vs, Ag/AgCl in 200–700 nm wavelength (**b**). Reproduced with permission [83]. Copyright 2020, Royal Society of Chemistry.

Another work was conducted by Qi and his team that aimed to prepare WS_2/BiOCl heterojunction using an in situ preparation method by stacking 1–2 μm on a 2–5 μm layer of WS_2 and used several analytical means such as XRD and EDS element mapping to reveal the crystallization of the prepared composite. The team synthesized the heterojunction with a varied mass ratio of WS_2 ranging as follows: 1%, 3%, 5%, 7%, and 9%. The study found that by increasing the mass ratio of WS_2, the visible light response range of BiOCl increases. The best degradation efficiency against MB was exhibited by 7%-WS_2/BiOCl, which is shown in TEM and HRTEM images in Figure 12a–c. This heterostructure reached 95.83% in 240 min. The outstanding performance of 7%-WS_2/BiOCl can be concluded from Figure 12d,e.

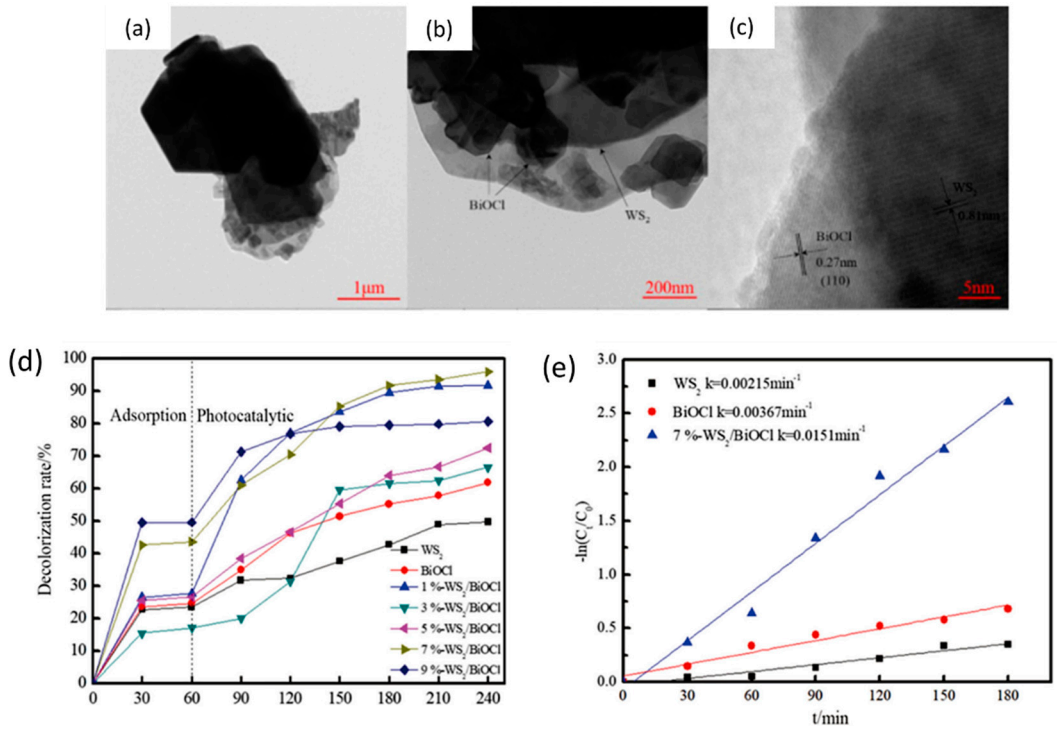

Figure 12. TEM and HRTEM images of the composite 7%-WS_2/BiOCl (**a**–**c**), photocatalytic decolorization rate plot of varied mass ratios of WS_2/BiOCl (**d**), kinetic analysis curve of WS_2, BiOCl, and 7%-WS_2/BiOCl (**e**). Reproduced with permission [84]. Copyright 2020, Springer Nature.

γ-$CsPbI_3$/WS_2

Zhang, Tai, Zhou, and others developed two different γ-$CsPbI_3$ nanocrystal (NCs)/WS_2 heterostructures with two different 2D morphologies of WS_2, which are nanoplates and few-layered nanosheets, and they were characterized using several techniques such as TEM (Figure 13a,b). This heterostructure helps to overcome the weaknesses of $CsPbI_3$ as a photocatalyst, such as the significant photoluminescence quenching and the existence of ligands attached to the surface of nanocrystals. The authors found that WS_2 provides a large surface area and abundant functional groups (e.g., C=O, -OH, C=C) on the surface, which facilitate bonding interaction with the precursors in the mixture solution and hence reduce the number of ligands and improve the nanocrystals of γ-$CsPbI_3$, which can be observed in Figure 13c that compares the photocatalytic degradation efficiency of γ-$CsPbI_3$ NCs, γ-$CsPbI_3$ NCs/WS_2 nanoplates, and γ-$CsPbI_3$ NCs/few-layered WS_2 nanosheets. Moreover, they concluded that γ-$CsPbI_3$ nanocrystals heterostructured with few-layered WS_2 nanosheets showed an improved photocatalytic activity due to the outstanding carrier-transport property introduced by WS_2 nanosheets. Consequently, this leads to producing more hydroxyl radicals to photodegrade methylene blue in high efficiency that reaches 100% in 30 min with no intermediate degradation products. Generally, the team offered a superior method for enhancing the photocatalytic activity of γ-$CsPbI_3$ NCs. In addition, the important role of tuning the surface interactions and carrier transport through 2D materials was successfully demonstrated.

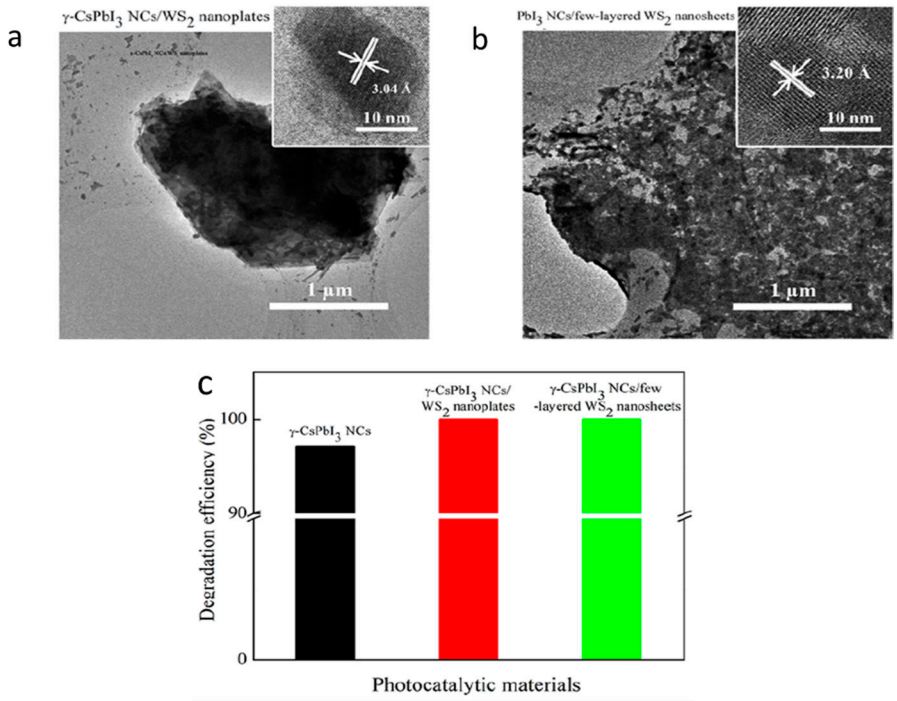

Figure 13. TEM images of γ-CsPbI3 NCs/WS2 nanoplates (**a**) and γ-CsPbI3 NCs/few-layered WS2 nanosheets (**b**), photocatalytic degradation efficiencies of the γ-CsPbI3 NCs, γ-CsPbI3 NCs/WS2 nanoplates, and γ-CsPbI3 NCs/few-layered WS2 nanosheets based on the intensity variation of MB dye at 653 nm (**c**). Reproduced with permission [85]. Copyright 2020, American Chemical Society.

WS2/g-C3N4

Tran, Truong, Nguyen, and others synthesized WS2/g-C3N4 composite photocatalysts varying in the amounts of WS2 and g-C3N4 using a facile calcination method that involved heating the mixtures of tungstic acid and thiourea considering that the relative content of WS2 in the composites decreases with increasing the amount of thiourea used in the mixture. The composites synthesized differed in the weight ratios of the precursors (tungstic acid and thiourea) as follows: 1:5, 1:7, and 1:10 to be denoted as nWCN, where n is equal to 5, 7, and 10, respectively. Figure 14a–e represents the SEM images of the synthesized WS2, g-C3N4, and the three composites. Generally, the fabricated composites showed enhanced photocatalytic activity in the degradation of methylene blue compared to the activity of each component separately. It was found that 7WCN exhibited the best photocatalytic activity among other heterostructures, which can be observed in Figure 14f of the photodegradation of MB using the fabricated composites. In addition, the authors observed a synergistic effect between WS2 and g-C3N4 in photocatalytic activity for the heterostructures synthesized.

Similarly, Nawaz, Goudarzi, Sarvanan, and Zarrin reported the preparation of z-scheme of g-C3N4/WS2 via one-pot hydrothermal synthesis without using a reducing agent. They attempted to synthesize different heterojunctions by changing the concentration of WS2 and keeping g-C3N4 to be as follows: CNW-0.5, CNW-1.0, and CNW-1.5, and they were characterized via several techniques including SEM as shown in Figure 15a–c. The study showed that the CNW-1.0 sample has improved charge mobility, and its transient photocurrent exhibited a prolonged lifetime of the charge carriers, using the Nyquist Plot. Moreover, Mott Schottky (MS) plots in Figure 15f–h showed the p-n junction formation of the heterostructure with a potential energy barrier at the junction. The average lifetime demonstrated by the time-resolved transient PL decay curves was 2.6 times higher for CNW-1.0 compared to WS2 alone. In addition, the same composite achieved 95.5% photocatalytic degradation for MB as the best composite among all samples as shown in Figure 14e, having ($O_2^{\bullet-}$) and ($^{\bullet}OH$) as the dominant radicals. The CNW-1.0 had

the highest photocurrent, which was 1.8 and 2.05 times higher than that of WS_2 and g-C_3N_4, respectively, as represented by the curve in Figure 15d. The researchers succeeded in providing a cost-effective photocatalyst using a Z-scheme mechanism with an improved photocatalytic activity for removing organic pollutants from water efficiently.

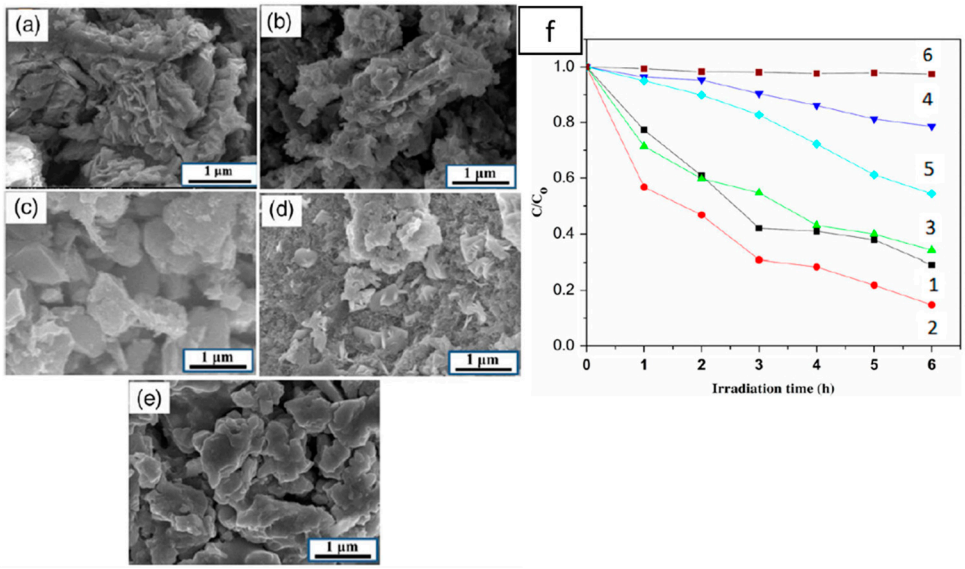

Figure 14. SEM images 5WCN (**a**), 7WCN (**b**), 10WCN (**c**), WS_2 (**d**), and g-C_3N_4 (**e**), Photocatalytic degradation of MB on 5WCN (1), 7WCN (2), 10WCN (3), WS_2 (4), g-C_3N_4 (5), and without photocatalyst (6) (**f**). Reproduced with permission [86]. Copyright 2018, John Wiley and Sons.

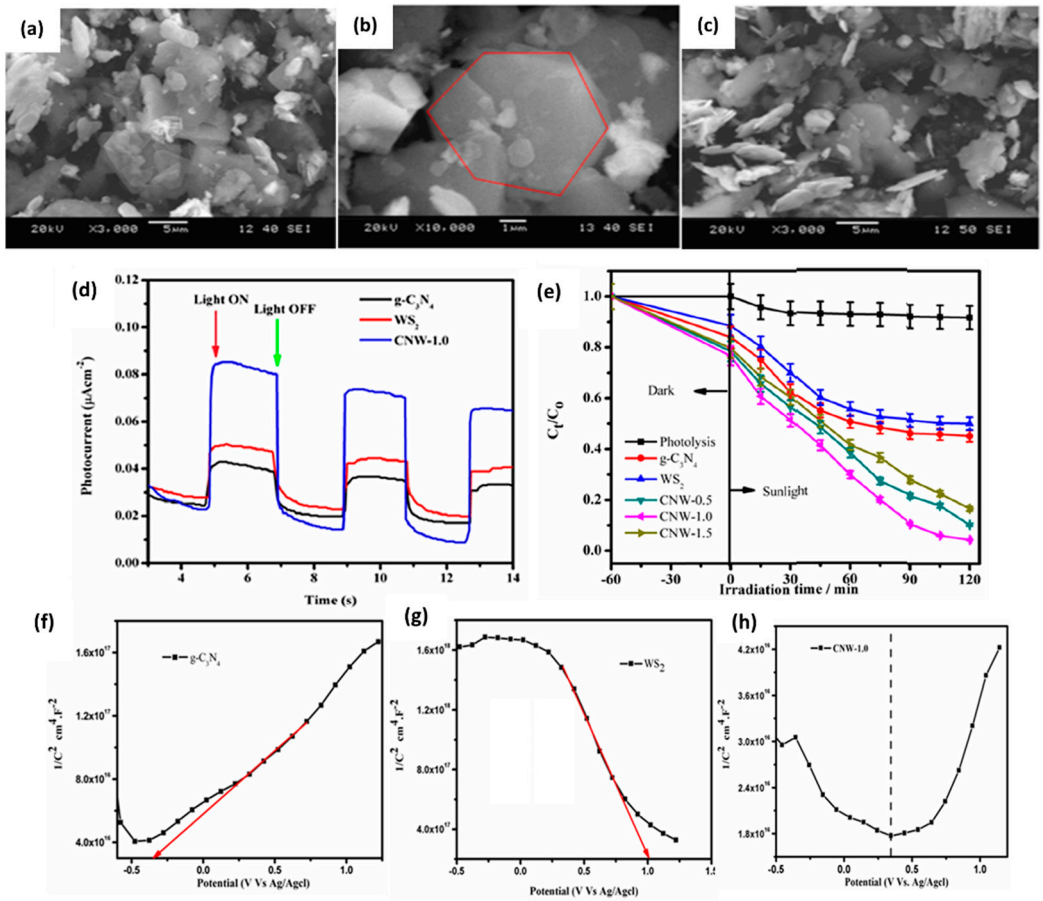

Figure 15. SEM images of CNW-0.5 (**a**), CNW-1.0 (**b**) (where the red line highlights the hexagonal crystal structure), CNW-1.5 (**c**), the curve of photocurrent vs. time of the synthesized g-C_3N_4, WS_2

and CNW-1.0 composite with on/off cycles under visible light (**d**), the photodegradation of MB with all samples at varying irradiation time (**e**), the MS plots of g-C_3N_4 (**f**), WS_2 (**g**), and CNW-1.0 (**h**). Reproduced with permission [20]. Copyright 2021, Elsevier.

Another work was conducted by Zeng, Ji, Su, and Zhang who prepared a heterogeneous WS_2/g-C_3N_4 composite photocatalyst using a facile ultrasound-assisted hydrothermal method varying in weight percentage of WS_2 and used different techniques to characterize the composites such as XRD (Figure 16a). It was used to regenerate NAD^+ to NADH photocatalytically, which was then used for the sustainable bioconversion of CO_2 to methanol with the aid of visible light irradiation. The study found that the fabricated WS_2/g-C_3N_4 composite with 5 wt% of WS_2 achieved the highest activity for methanol production nearly 7.5 times higher than that produced by pure g-C_3N_4. The same composite also achieved about 100% of RhB removal ratio as a photocatalyst in 1 h, which is 2.6 times higher than that of g-C_3N_4 alone as can be seen in Figure 16b. According to this study, the enhancement achieved by the fabricated heterojunction was attributed to the formation of a heterojunction interface between WS_2 and g-C_3N_4, which provides an enhancement of the photo-harvesting efficiency and decreases the recombination of electrons and holes.

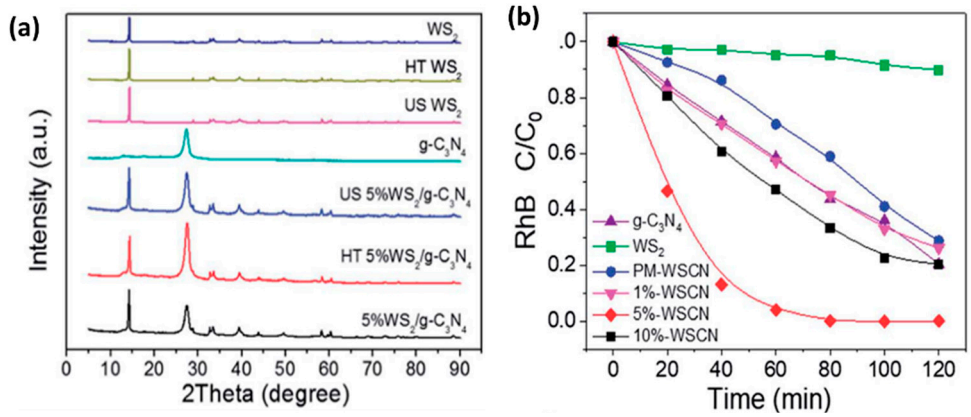

Figure 16. XRD patterns of all fabricated samples (**a**), photocatalytic degradation of RhB against the prepared samples under visible light irradiation (**b**). Reproduced with permission [87]. Copyright 2018, Royal Society of Chemistry.

WS_2/Fe_3O_4

Merci, Saljooqi, Shamspur, and Mostafavi designed and synthesized Fe_3O_4 and WS_2 nanoparticles on or in the pores of the prepared mesoporous material called KIT-6 (KIT: Korea Institute of Science and Technology) to form the photocatalyst (KIT-6/WS_2-Fe_3O_4) using a hydrothermal method, and it is shown in the FE-SEM image in Figure 17a. The material worked well as a photocatalyst under visible light irradiation for the degradation of representative chlorpyrifos (CP), which is an organophosphorus pesticide. According to the study, the good performance of the fabricated photocatalyst is due to its high specific surface area and relatively low recombination rate of hole-electron pairs caused by the synergic effect between KIT-6, Fe_3O_4, and WS_2. The authors used a central composite design with response surface methodology to study the effects of several variables such as chlorpyrifos concentration, KIT-6/WS_2-Fe_3O_4 nanocatalyst amount, pH, and the irradiation time on chlorpyrifos degradation efficiency. Figure 17b represents the contour and 3D surface plots of the interaction between pH value and the amount of the photocatalyst with fixing time and CP concentration. They also determined the optimum conditions for the CP degradation to be as follows: 50 mg of the nanocatalyst and 7.2 ppm CP solution with pH equals 6 and a time duration of 52 min. Under the mentioned optimum conditions, the material achieved 91% degradation of CP.

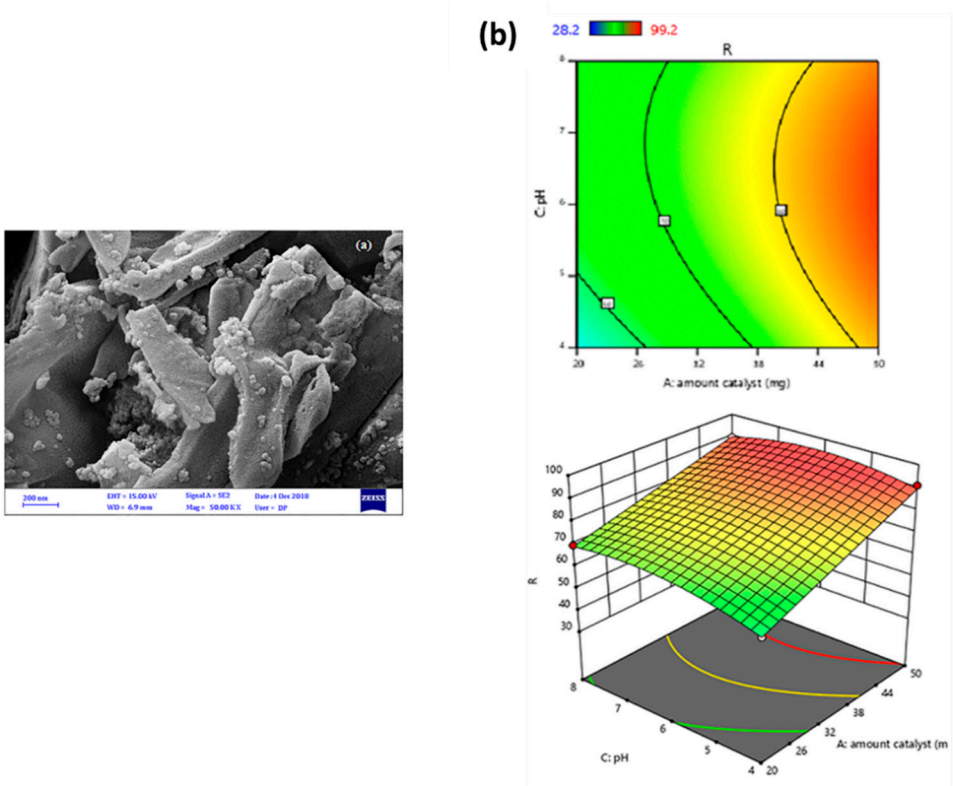

Figure 17. FE-SEM image of KIT-6/WS_2-Fe_3O_4 nanocomposite (**a**), contour and 3D surface plots of the degradation efficiency percentage by the relationship between the composite amount (mg) and pH value (**b**). Reproduced with permission [88]. Copyright 2020, John Wiley and Sons.

WS_2/MoS_2

Zhao, Liu, Zhang, and others succeeded in constructing a series of WS_2-MoS_2 composites with different phase ratios through a large-scale approach. They synthesized hexagonal-phase structured WS_2 by annealing the commercial powders of W and S in the presence of argon, whereas MoS_2 was synthesized using the hydrothermal method onto the surface of WS_2. SEM technique was used among several characterization techniques as presented in Figure 18a–c. The authors studied the optoelectronic properties of the heterostructure synthesized and found out that it can present more active sites and better separation of carriers than pure WS_2 and MoS_2. Furthermore, 4WS_2-96MoS_2 achieved the best photocatalytic degradation performance as shown in Figure 18d and a complete photodegradation of MB in 150 min. Moreover, 4WS_2-96MoS_2 showed an outstanding photoresponse behavior compared to both MoS_2 and WS_2 separately.

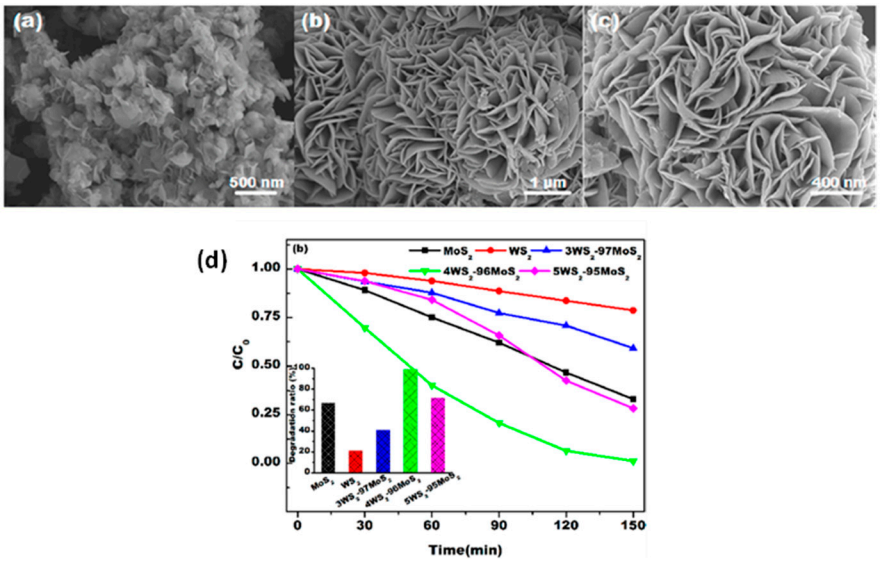

Figure 18. SEM images of WS_2 (**a**), MoS_2 (**b**), $4WS_2$-$96MoS_2$ (**c**), photocatalytic degradation profile of MB in the presence of the prepared samples (**d**). Reproduced with permission [89]. Copyright 2019, American Chemical Society.

Luo, Dong, Lu, and others reported a facile and green method to fabricate few-layered WS_2 suspensions at a large scale via a direct exfoliation of commercial WS_2 powders in a mixture of water and ethanol. After that, they grew MoS_2 nanoflakes onto WS_2 by an in situ hydrothermal reaction to achieve a novel 2D WS_2/MoS_2 composite. The researchers used different concentrations of WS_2 suspensions relative to water (S/W) as follows: 3/7, 1/1, 7/3, and 4/1. Figure 19a is an SEM image of WS_2/MoS_2 (S/W: 7:3). The prepared material exhibited an outstanding performance as a photocatalyst for the photodegradation of organic dyes such as RhB and MB reaching 93% and 85% removal in 90 min, respectively, which was attributed to the heterostructure effect, which results in distinctive electronic, optical, catalytic properties, as well as the matching energy band structure between WS_2 and MoS_2 for efficient separation of photogenerated electron-hole pairs. In addition, the 2D heterostructure offers an effective interaction between the nanosheets and provides more active sites for the photocatalytic process. Specifically speaking, WS_2/MoS_2 (7/3 S/W) showed the highest degradation rate, which is five times that of bare MoS_2, which can be seen in Figure 19b. The mentioned study suggested an effective solution for this environmental issue using a 2D heterostructured photocatalyst, as well as offered new insights into the synthesis and feasible applications of 2D layered TMDs.

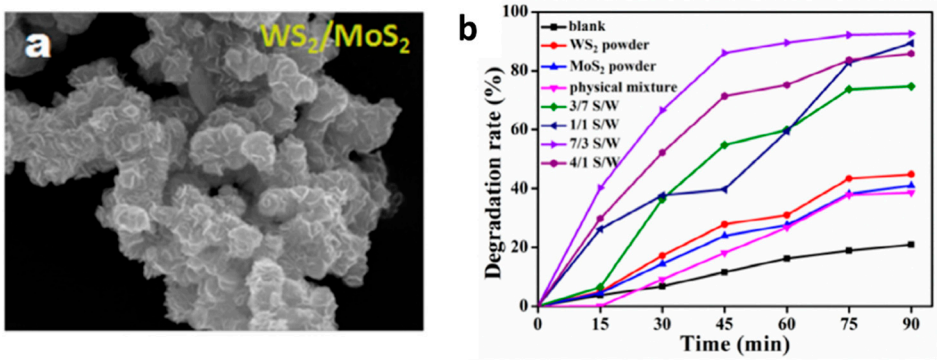

Figure 19. SEM image of WS_2/MoS_2 (S/W: 7:3) (**a**), photocatalytic degradation activities of the prepared samples against RhB (**b**). Reproduced with permission [90]. Copyright 2018, Elsevier.

$WS_2/MoS_2/BiOCl$

Qi, Liu and Ma, and Xu prepared $WS_2/MoS_2/BiOCl$ (WMB) photocatalysts via in situ synthesis method, which was found to overcome the challenge of fast recombination of photogenerated carriers that usually takes place when using two-dimensional layered transition metal chalcogenides as photocatalysts. Furthermore, the authors suggest that the incorporation of WS_2/MoS_2 increased the absorption range of BiOCl, lowered the energy needed for photogenerated charge transfer, and narrowed its band gap. They prepared different photocatalysts with various ratios of WS_2/MoS_2 and BiOCl (1%-WMB, 3%-WMB, 5%-WMB, 7%-WMB, and 9%-WMB). Several characterization techniques were used such as SEM, and Figure 20a represents an SEM image of 7%-WMB. As can be concluded from Figure 20b, the best photodegradation performance on methylene blue was achieved by 7%-WMB with an efficiency of 99.36% at 240 min.

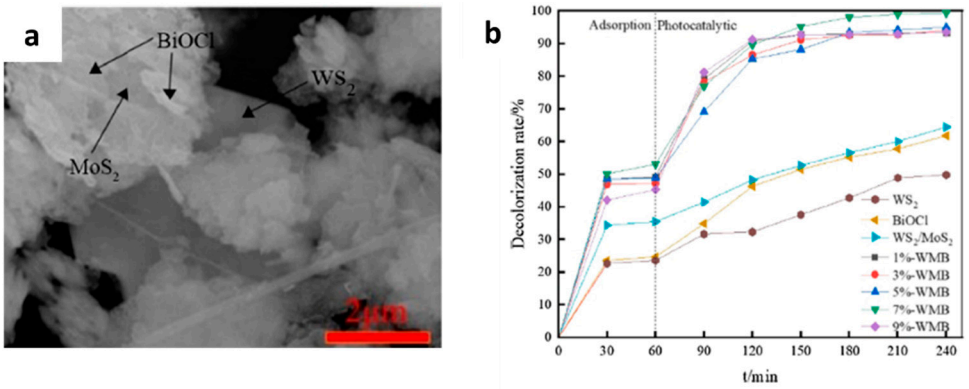

Figure 20. SEM image of 7%-WMB (**a**), curve of photocatalytic decolorization rate of WMB photocatalysts (**b**). Reproduced with permission [91]. Copyright 2021, Elsevier.

WS_2/WO_3

Barakat, and his team fabricated a tungsten oxide (WO_3)/disulfide (WS_2) coupled polyaniline (PANI) (WO_3/WS_2/PANI) heterojunction nanohybrid photocatalyst via hydrothermal method using L-Cysteine as a sulfurization agent used for the degradation of 2-chlorophenol (2-CP) in water. The prepared heterojunction was characterized using TEM and HR-TEM as shown in Figure 21a,b, in addition to other techniques such as XRD. The study found that adding PANI to WO_3/WS_2 creates a synergistic effect on photocatalytic properties, which is attributed to its enhanced light-harvesting properties, as well as the band gap energy suppression. The outstanding photocatalytic performance of the prepared photocatalyst is shown in Figure 21c. The authors concluded that the photocatalytic activity of the fabricated catalyst on 2-CP depends on irradiation time, 2-CP concentration, and pH value. By decreasing the initial concentration of 2-CP from 50 to 10 mg/L, the photocatalytic degradation increased from 83% to 100%. Moreover, the decomposition of 2-CP by WO_3/WS_2/PANI involved the reactive species $O_2^{\bullet-}$, $^{\bullet}OH$, and h^+ in the photocatalytic mechanism as suggested by Figure 21d. Kinetically, the degradation of the pollutant by the fabricated catalyst followed the first-order kinetic model. The ternary nanohybrid photocatalyst exhibited reusability after five cycles, in addition to the outstanding catalytic activity. This study added significant perceptions into the coupling method used to construct a visible light-driven photocatalyst that is reusable, recyclable and convenient for degrading organic substances in wastewater.

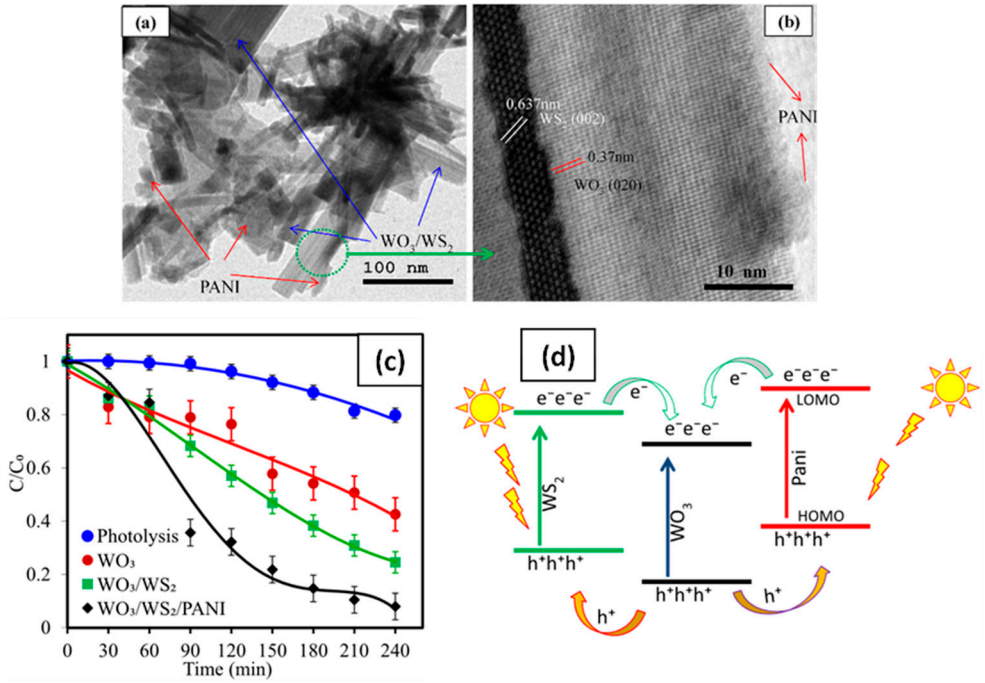

Figure 21. TEM (**a**) and HR-TEM images (**b**) of WO_3/WS_2/PANI nanocomposite, photocatalytic degradation of 2-CP using the prepared materials (**c**), schematic diagram for the mechanism of producing and separating the electron/hole pairs at the fabricated heterojunction WO_3/WS_2/PANI (**d**). Reproduced with permission [92]. Copyright 2022, Elsevier.

WS_2/ZnO

Yu, Chen, Mei, and others prepared the reduced graphene oxide/WS_2/Mg-doped ZnO composite (rGWMZ) by electrostatic self-assembly and coprecipitation methods. The presence of WS_2 helped in improving the dispersion of reduced graphene oxide and in enhancing the photocatalytic property of reduced graphene oxide/Mg-doped ZnO composite (rGMZ). This article reported that the photocatalytic efficiency of rGWMZ composites is three-fold compared with that of rGMZ composites. TEM and HR-TEM images of both composites are shown in Figure 22a–d.

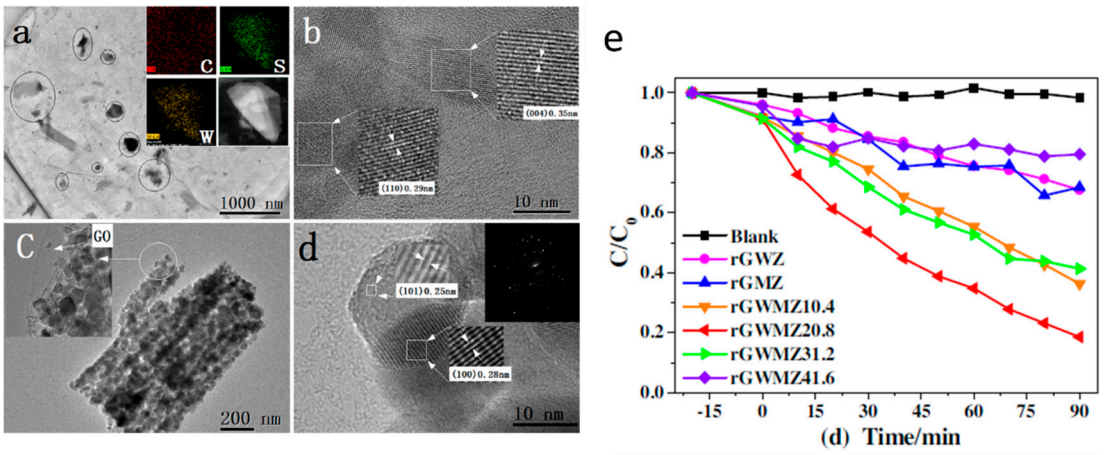

Figure 22. TEM (**a**) and HR-TEM image (**b**) of rGO/WS_2, TEM (**c**) and HR-TEM image (**d**) of rGWMZ 20.8, photocatalytic activity of the prepared samples under visible light irradiation (**e**). Reproduced with permission [93]. Copyright 2017, Elsevier.

The prepared rGMZ composite achieved 95% degradation of Rhodamine B (RhB) in 15 min under UV light and 90% in 90 min under simulated solar light when the WS2/rGO

weight% is 20.8% and the calcination temperature is 500 °C. It was concluded that rGWMZ 20.8 exhibited the best photocatalytic activity among all prepared samples as represented by Figure 22e. Furthermore, the researchers stated that the rGWMZ exhibits larger capacitance and smaller resistance than rGMZ. The improved photocatalytic activity exhibited by rGWMZ is assigned to the specific surface area, electrical conductivity, and charge storage ability resulting from the synergistic effect of the combination of rGO and WS_2 nanosheets.

In addition, Zhang, Qiu, Rong, and others synthesized a highly efficient zinc oxide/graphene-like tungsten disulfide nanosheet (ZnO/WS_2) via a facile two-step method. The photocatalyst was used to degrade Rhodamine B (RhB) dye under 500 W tungsten lamp radiation, and absorption spectra were constructed in the presence of the prepared samples as shown in Figure 23b. The study showed that adding WS_2 enhanced the photocatalytic activity of the catalyst and achieved 95.71% of degradation efficiency in 120 min under visible light radiation. In addition, the fabricated photocatalyst exhibited high stability as it maintained high photocatalytic activity after four successive recycles. The graphene-like WS_2 sheets were folded gossamer according to the TEM images (Figure 23a), which contributes to the photocatalytic activity. The authors conducted a UV–Vis DRS analysis by which they concluded that WS_2 has a narrow band gap that may improve the visible-light absorption of pure ZnO photocatalysts. It was reported that the enhanced photocatalytic activity of the synthesized photocatalyst is because of the overlapping of the energy levels of both WS_2 and ZnO that played a role in the charge separation. Moreover, the separation of the photo-induced electron-hole pairs could be promoted by the hydrothermal conditions during the synthesis process, which helps in accelerating the photocatalytic degradation of RhB.

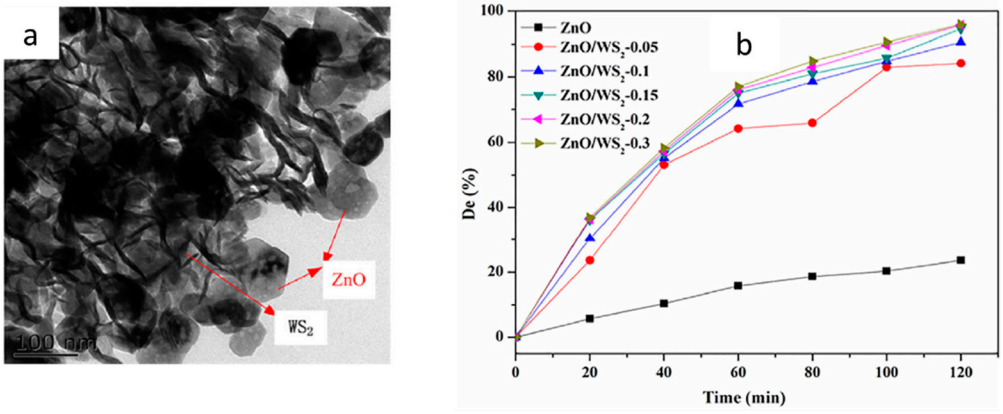

Figure 23. TEM image of ZnO/WS_2 under magnification 97,000 times (**a**), absorption spectra of RhB with all prepared samples (**b**). Reproduced with permission [94]. Copyright 2017, John Wiley and Sons.

WS_2/TiO_2

Cho, Chang-Jian, Zheng, and others reported the preparation of a visible light-responsive photocatalyst based on TiO_2/WS_2 by a combination of liquid exfoliation and solvothermal methods. The prepared photocatalyst was confirmed using various characterization techniques such as XRD as shown in Figure 24a. The prepared composite showed a larger surface area and a wider range of optical absorption than bare TiO_2, in addition to the decreased rate of recombination of the photogenerated electron/hole pairs. The photoinduced electrons readily transferred from WS_2 to TiO_2 because the conduction band of WS_2 was at a higher energy level than that of TiO_2. Furthermore, the WS_2 nanoparticles worked as a sensitizer to TiO_2, and hence, it expanded the amount of useable solar spectrum from the UV to the visible. The study revealed that the energy band levels of the heterojunction between the TiO_2 and WS_2 were suitable for charge transfer, and this achieved the ultraviolet photoelectron spectroscopy. The photocatalytic activity of the

fabricated photocatalyst was studied through the degradation of methylene blue under a white light emitting diode (LED), where the optimal content of WS_2 was 3.0 weight% as represented by Figure 24b. The authors suggested that the TiO_2/WS_2 composite could contribute to biomedical applications due to the high biocompatibility, as it did not affect cellular proliferation or morphology.

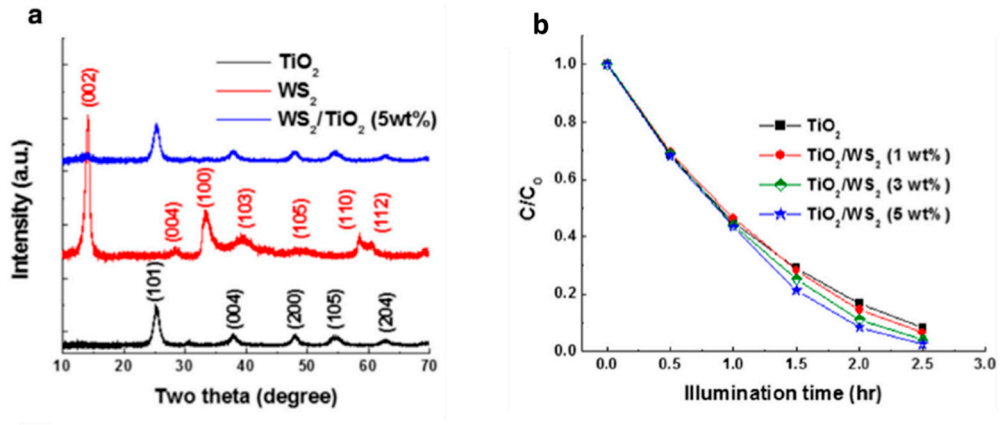

Figure 24. XRD patterns of as-prepared TiO_2/WS_2 composites (**a**), photodegradation of MB with TiO_2/WS_2 photocatalyst at different WS_2 wt% under UV irradiation (**b**). Reproduced with permission [95]. Copyright 2018, Elsevier.

In another work, Wu and his team fabricated novel WS_2 nanodots-modified TiO_2 nanotubes (TNT/WND) composites using a one-pot hydrothermal method. The preparation method involved growing WS_2 nanodots on the inner wall of the TiO_2 nanotube as can be observed in the TEM and HR-TEM images in Figure 25a,b. The composite exhibited superior photocatalytic activity evaluated by the photodegradation of RhB under visible light as represented by the plot in Figure 25c.

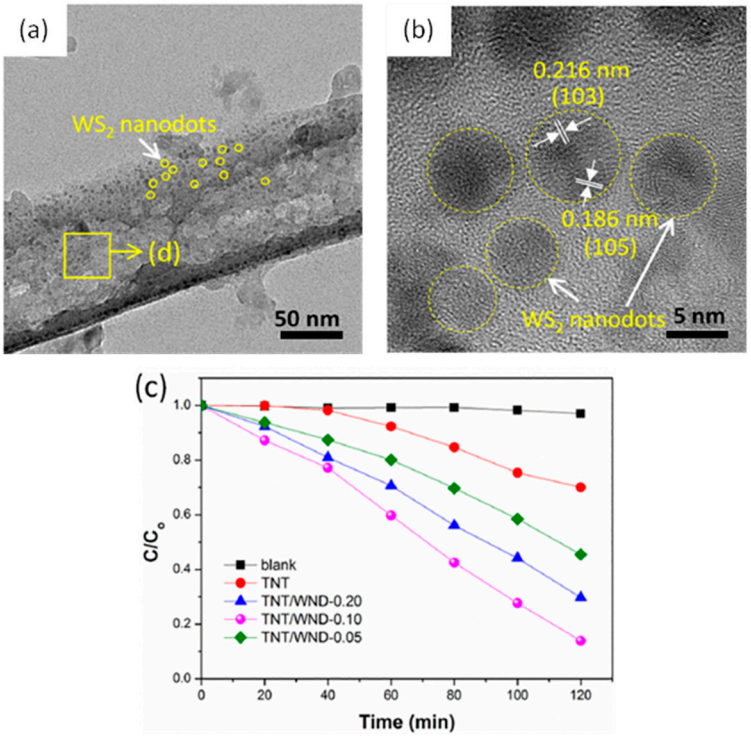

Figure 25. TEM (**a**) and HR-TEM (**b**) images of TNT/WND-0.10, photocatalytic degradation of RhB in the presence of as-prepared samples under visible light irradiation (**c**). Reproduced with permission [96]. Copyright 2019, Elsevier.

That is because of the synergistic effect resulting from the low recombination rate of the photogenerated electron-hole pairs as well as the high specific area. TNT/WND-0.10 composite achieved the highest removal percentage of RhB of 86.1% in 120 min, which is 2.7 times higher than that of pure TiO_2 nanotubes.

Table 4 summarizes the recent studies on organic substances photodegradation using WS_2-based nanomaterials.

Table 4. WS_2-based nanomaterials for organic substances photodegradation.

WS_2-Based Photocatalyst	Organic Pollutants	Removal Efficiency	Ref.
Few-layer WS_2 nanosheets	BG	95%, 10 h	[19]
Inorganic fullerene (IF)-type WS_2 nanoparticles	MG	712%	[22]
Hexagonal-shaped WS_2 platelets	RhB	98%, 105 min	[47]
WS_2 nanosheets, WS_2 nanorods	MB	$WS_{2(NS)}$: ~100%, 60 min $WS_{2(NR)}$: ~50%, 60 min	[77]
	4-CP	$WS_{2(NS)}$: ~100%, 120 min $WS_{2(NR)}$: ~69%, 120 min	
WS_2 (e-h-WS_2)	MO	99%, 60 min	[78]
	CR	99%, 110 min	
	RhB	99.9%, 100 min	
	PR	99%, 110 min	
WS_2/Ag	Evans blue	Dye rejection rate: 90.2%	[79]
AgI/WS_2	RhB	91.2%, 30 min	[80]
WS_2/$Bi_2O_2CO_3$	LR5B	91%, 90 min	[81]
WS_2/BiOBr	RhB	95%	[82]
BiOCl/WS_2	MG	99%, 60 min	[83]
BiOCl/WS_2	MB	95.83%, 240 min	[84]
γ-$CsPbI_3$/WS_2	MB	100%, 30 min	[85]
WS_2/g-C_3N_4	MB	85.3%, 6 h	[86]
WS_2/g-C_3N_4	MB	95.5%, 2 h	[20]
WS_2/g-C_3N_4	RhB	100%, 1 h	[87]
WS_2/Fe_3O_4	CP	91%	[88]
WS_2/MoS_2	MB	100%, 150 min	[89]
WS_2/MoS_2	RhB	93%, 90 min	[90]
	MB	85%, 90 min	
WS_2/MoS_2/BiOCl	MB	99.36%, 240 min	[91]
WS_2/WO_3	2-CP	100%	[92]
WS_2/ZnO (rGWMZ)	RhB	100%, 5 min	[93]
ZnO/WS_2	RhB	95.71%, 120 min	[94]
WS_2/TiO_2	MB	100%, 480 min	[95]
WS_2 nanodots-modified TiO_2 nanotubes	RhB	86.1%, 120 min	[96]

Brilliant Green (BG), Malachite green (MG), rhodamine B (RhB), methylene blue (MB), 4-chlorophenol (4-CP), methyl orange (MO), Congo red (CR), phenol red (PR), Lanasol red 5B (LR5B), chlorpyrifos (CP), 2-chlorophenol (2-CP).

4.2. Microorganisms' Disinfection

Microbial pollution is among the most popular problems, as it is directly related to health and the environment [97]. Wastewater treatment plants cannot usually remove the pathogenic microorganisms because of the shortage in financial resources, which causes hazardous effects on public health [98]. Currently, pathogenic microorganisms contaminating water such as viruses, fungi, and bacteria and their corresponding infections are of particular concern. It is known that pathogens infections have been creating disasters such as cholera, which is caused by *Vibrio cholerae*, and plague, which is caused by *Yersinia pestis*. The enterotoxin-genic *Escherichia coli*, which causes diarrheal illness and passes through contaminated water, kills about 1.3 million children annually [99,100]. Referring to the WHO Guidelines for drinking water quality, drinking water is considered safe if it is free from fecal organisms including *Escherichia coli*, *Clostridium perfringens*, *Enterococcus* spp., Total coliforms, Thermotolerant coliforms [101]. The antibacterial photocatalytic mechanism begins by damaging the bacterial cell membrane, which causes damage to the internal components of the bacterial cell consequently. After that, the photocatalytic reactions will oxidize the remaining parts of the leaked bacterial cell [102,103].

4.2.1. WS_2 Monolayer

Thakur, Sharma, Vaish, and Balakrishnan prepared a uniform large-area WS_2 monolayer through chemical vapor deposition (CVD) on a sapphire (Al_2O_3) substrate for the disinfection of *E. coli* bacteria as illustrated in Figure 25a, and they reported optical images of the products as represented by Figure 26b–d.

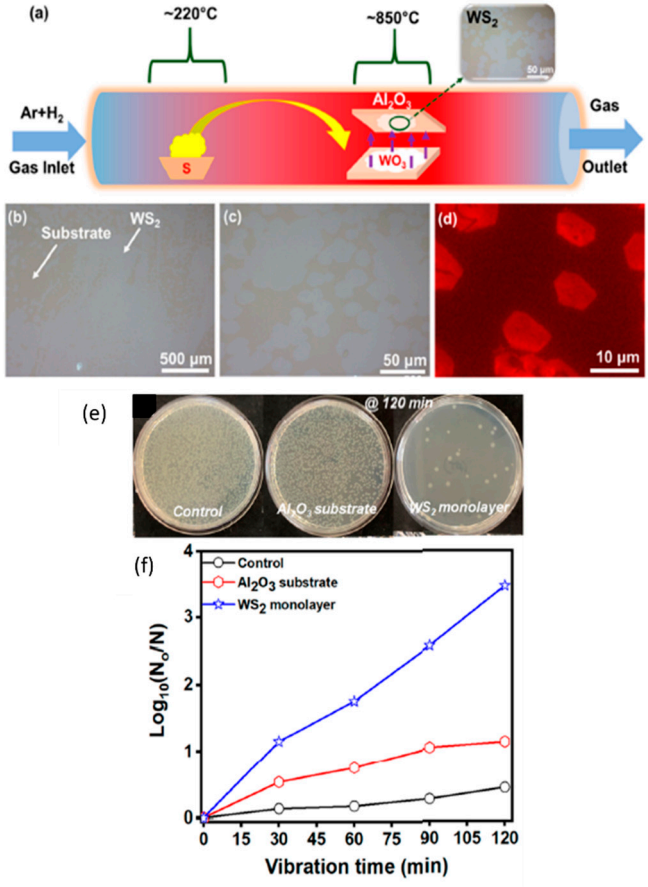

Figure 26. CVD growth process scheme (**a**), optical image of the large-scale growth of WS_2 monolayer (**b**), optical images of high magnification for individual areas of WS_2 (**c**), FL image of WS_2 monolayer, antibacterial performance of the prepared WS_2 monolayer (**d**), optical image of a colony

of *E. coli* bacterial cell (**e**); log reduction of CFUs/mL of a colony of *E. coli* bacterial cell with time (**f**). Reproduced with permission [53]. Copyright 2021, American Chemical Society.

The authors stated that the piezoelectric polarization enhanced the separation of electrons and holes to produce more reactive oxygen species (ROS) that contribute to the degradation of bacteria by preventing DNA replication, and the effect of the fabricated WS_2 on the bacteria can be observed in Figure 26e,f.

4.2.2. $Ag_2S@WS_2$

Lin and his team synthesized the photocatalyst $Ag_2S@WS_2$ as a new kind of antibacterial agent by decorating exfoliated WS_2 nanosheets with Ag_2S nanoparticles via in situ growth by a simple solution method at room temperature. Figure 27a is an SEM image of the $Ag_2S@WS_2$ 20% composite, which exhibited the best photocatalytic activity among fabricated composites. The synthesized composite showed an excellent photocatalytic property due to the effective separation of photoinduced electrons and holes. The fabricated heterostructure between Ag_2S nanoparticles and WS_2 nanosheets enhanced the electron mobility and controlled the photogenerated electron-hole pairs recombination. As a result of the synergistic effect of photocatalytic properties, $Ag_2S@WS_2$ 20% achieved a highly effective antibacterial activity in 20 min, which is 99.93% and 99.84% toward *Staphylococcus aureus* (*S. aureus*) and *Escherichia coli* (*E. coli*), respectively, as can be concluded from Figure 27b,c. The result of this study introduced $Ag_2S@WS_2$ as a promising photocatalyst for effective disinfection, as it was found that it is noncytotoxic according to the in vitro culture test.

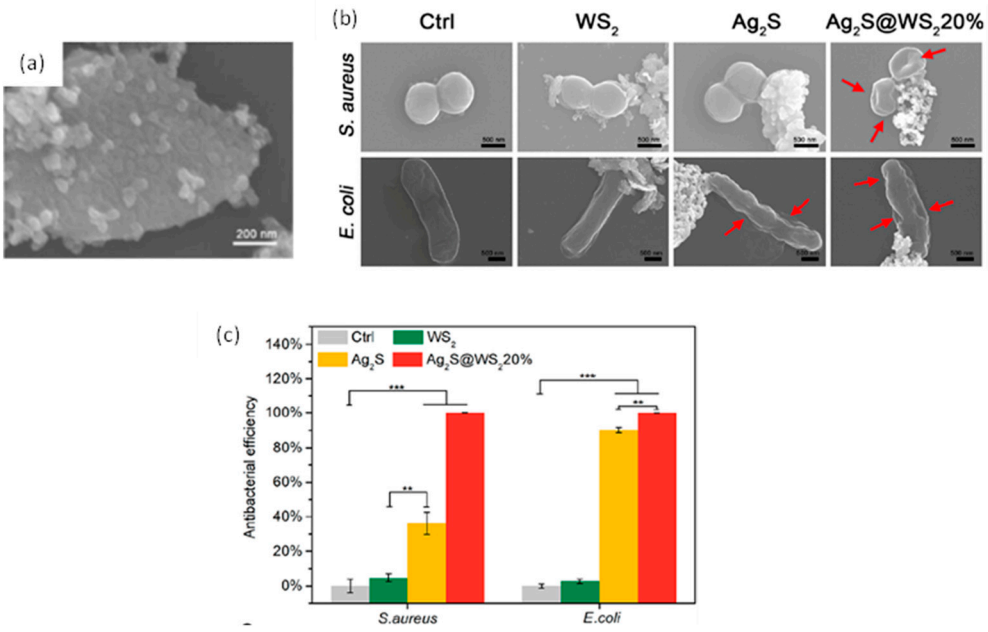

Figure 27. SEM image of $Ag_2S@WS_2$ 20% composite (**a**), SEM images of treated bacterial cells by the samples: control, WS_2, Ag_2S and the composite $Ag_2S@WS_2$ 20% (**b**), the antibacterial efficiency of the samples after 20 min irradiation against *S. aureus* and *E. coli* (**c**). Reproduced with permission [104]. Copyright 2019, American Chemical Society.

4.2.3. Graphene oxide/WS_2/Mg-doped ZnO

Chen, Yu, Liu, and others synthesized three-dimensional (3D)-reduced graphene oxide/WS_2 nanosheet/Mg-doped ZnO nanohybrid (rGOWMZ) by the layer-by-layer electrostatic assembly method. The morphology of the composite is layers of small nanoparticles as shown in the HR-SEM image in Figure 28a. The composite achieves better antibacterial activity in than dark than the reduced graphene oxide/Mg-doped ZnO composites

(rGOMZ) hybrid, as can be seen in Figure 28b. The study attributes the enhancement in the antibacterial activities to defect and efficient electron-hole separation. The antibacterial activity was evaluated against *S. aureus* and *E. coli* via the agar diffusion method. This work proves that the produced 3D rGOWMZ photocatalyst can be implemented in environmental remediation purposes, sunlight-driven photocatalysis and the photovoltaics field.

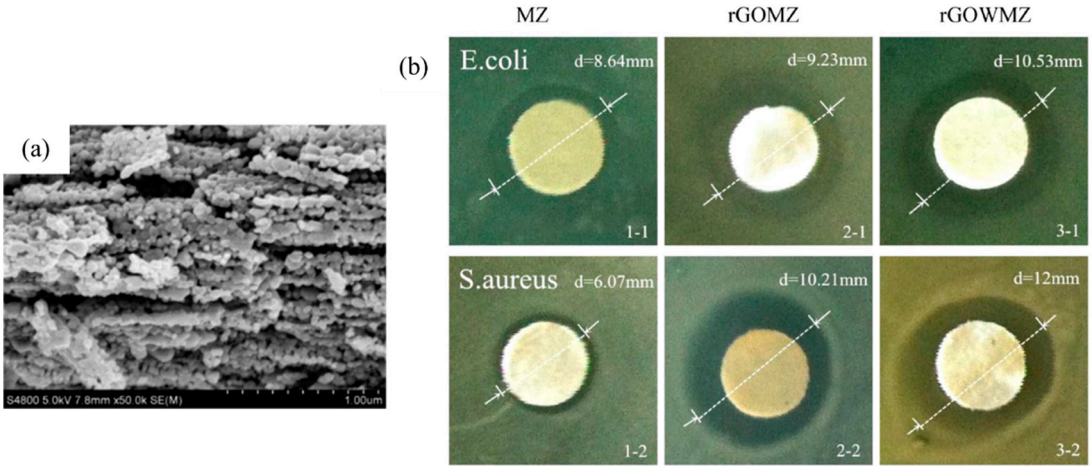

Figure 28. HR-SEM image of rGOWMZ composite (**a**), the antibacterial activity of Mg/ZnO, rGOMZ, and rGOWMZ samples toward *E. coli* and *S. aureus* (**b**). Reproduced with permission [105]. Copyright 2017, Elsevier.

4.2.4. WS_2/Ag Nanoparticle

Kumar, Kataria, Roy, and others synthesized a WS_2 monolayer using chemical vapor deposition (CVD), then decorated it with Ag nanoparticles with roughly 42% areal coverage on SiO_2/Si substrate, and then used the composite for water disinfection. The XRD pattern shown in Figure 29a suggests the successful formation of WS_2 having a certain orientation. The WS_2 monolayer decorated with 10–15 nm Ag nanoparticles achieved high antibacterial efficiency of almost 96% against Gram-negative *E. coli* bacteria in water as represented by Figure 29b. The study used fluorescent light to create electrons and holes in WS_2, and hence, the disinfection mechanism was found to be photocatalytic in nature. To enhance the antibacterial activity of WS_2, Ag nanoparticles were added; thus, the charge transfer takes place from WS_2 to Ag nanoparticles, and the recombination is suppressed. The excited electrons in WS_2 cause an increase in reactive oxygen species (ROS) generation, which is confirmed by the observed charge transfer and photoluminescence quenching along with the antibacterial activity. Moreover, the study observed a direct correlation between the areal coverages of WS_2 in Ag/WS_2/SiO_2/Si samples and the corresponding antibacterial efficiencies. However, further investigation of disinfection rate and durability of other WS_2-based nanocomposites under fluorescent light exposure should be studied for water disinfection purposes in future works.

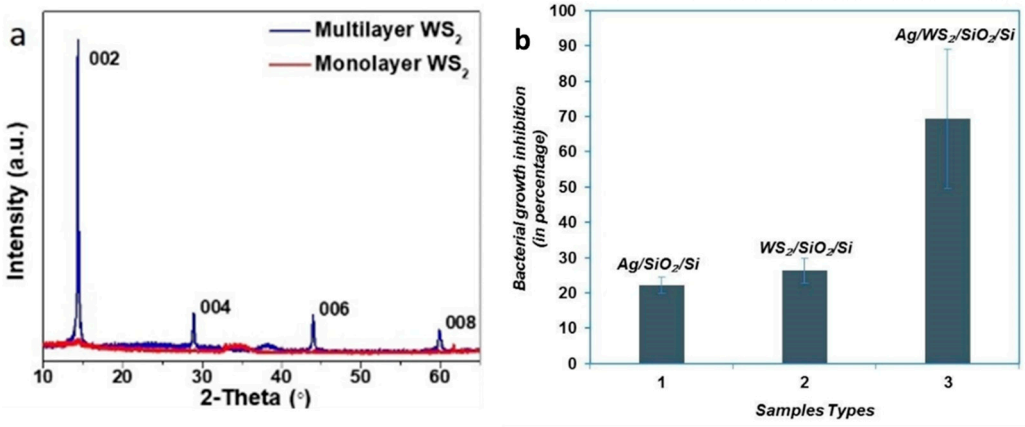

Figure 29. XRD patterns of monolayer and multilayer WS_2 (**a**), graphical statistics for bacterial growth inhibition percentage according to the control sample (**b**). Reproduced with permission [106]. Copyright 2018, John Wiley and Sons.

4.2.5. PMS/WS_2/Fe^{3+}

Luo, Liu, and Cheng reported the fabrication of the co-catalysts WS_2 and Fe^{3+} for the activation of peroxymonosulfate (PMS) to be used for the inactivation of *E. coli* bacteria (Figure 30a–c), where the inactivation rate achieved was 97.3% in one minute in a wide range of pH. The study concluded that WS_2 participates in the activation of PMS by accelerating the Fe^{3+}/Fe^{2+} cycle. In addition, the log N value of *E. coli* decreased from 8.9 to 4.6 in 5 min. The system PMS/WS_2/Fe^{3+} was found to generate the radicles SO_4^{-} and $HO^{\bullet-}$; however, the role of SO_4^{-} was more significant. This study suggests a promising technology for activating PMS and employing it in a photocatalytic system along with WS_2 in order to inactivate pathogenic bacteria effectively.

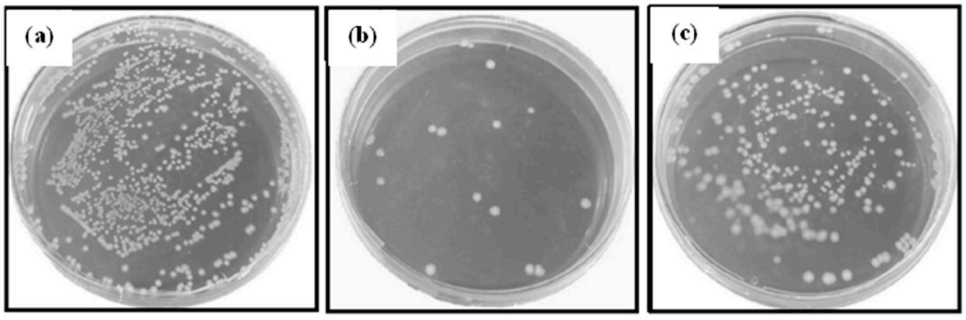

Figure 30. Photo images of *E. coli* inhibition at different conditions: blank (untreated) (**a**), PMS/WS_2/Fe^{3+} (**b**), PMS/WS_2 (**c**). Reproduced with permission [107]. Copyright 2021, Elsevier.

4.2.6. CS/WS_2/Pd

Kasinathan, Marimuthu, Murugesan, and others fabricated WS_2 nanosheets in addition to chitosan and palladium (CS/WS_2/Pd) and studied its antibacterial activity against Gram-positive bacteria including *Bacillus subtilis* and *Staphylococcus aureus*, as well as Gram-negative bacteria including *Klebsiella pneumoniae* and *Escherichia coli*.

Figure 31a shows the XRD spectra of the synthesized samples. The XRD pattern of WS_2 nanosheets indicates that they have a crystalline hexagonal structure. The most significant effect of the composite was on *E. coli*, and it is represented by Figure 31c. The composite was synthesized via a liquid exfoliation process, and the Pd nanoparticles with an average particle size of 10–15 nm were anchored onto the surface of the CS/WS_2 composite, which was revealed by the TEM and SEM analysis (Figure 31b). The nanocomposite is thermally stable, and that was confirmed by the TGA analysis, which showed that the Pd nanoparticles were effectively immobilized on the CS/WS_2 composite. In addition,

the X-ray diffraction analysis revealed the hexagonal structure of the WS_2, as well as the modification of the WS_2 lattice caused by the loading of Pd nanoparticles, which resulted in a peak change.

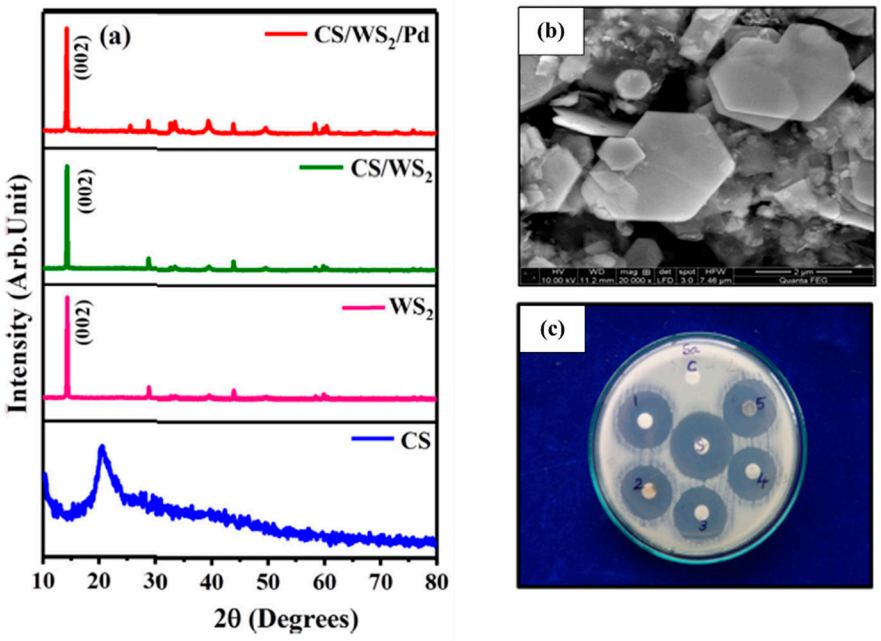

Figure 31. XRD spectra of all samples (**a**), SEM images of CS/WS_2/Pd composite (**b**), photographic representation of antibacterial activity of CS/WS_2/Pd against *E. coli* (**c**). Reproduced with permission [108]. Copyright 2021, Elsevier.

4.2.7. CS/WS_2/Ru

Kasinathan, Marimuthu, Murugesan, and others fabricated an eco-friendly nanocomposite of chitosan and a few layers of WS_2 implanted with ruthenium nanoparticles (CS/WS_2/Ru). The composite was synthesized via a liquid exfoliation route, and it showed an outstanding antibacterial action against Gram-positive *S. aureus* and Gram-negative *E. coli* bacteria as represented by Figure 32c. Moreover, the composite exhibited a significant anticancer action toward MCF-7 cancer cells, and it has low toxicity. Different characterization techniques including Raman, XRD, FTIR, and TGA showed that the Ru NPs were successfully implanted on the CS/WS_2 composite's surface. The presence of a high-density diffraction peak (002) is an indication of multi-layered WS_2 nanosheets being formed, and the increased intensity indicates the formation of a 2D structure (Figure 32a). SEM and TEM were also used to confirm the presence of Ru NPs, and the particle size ranges between 5 to 20 nm. An SEM image of the composite is shown in Figure 32b.

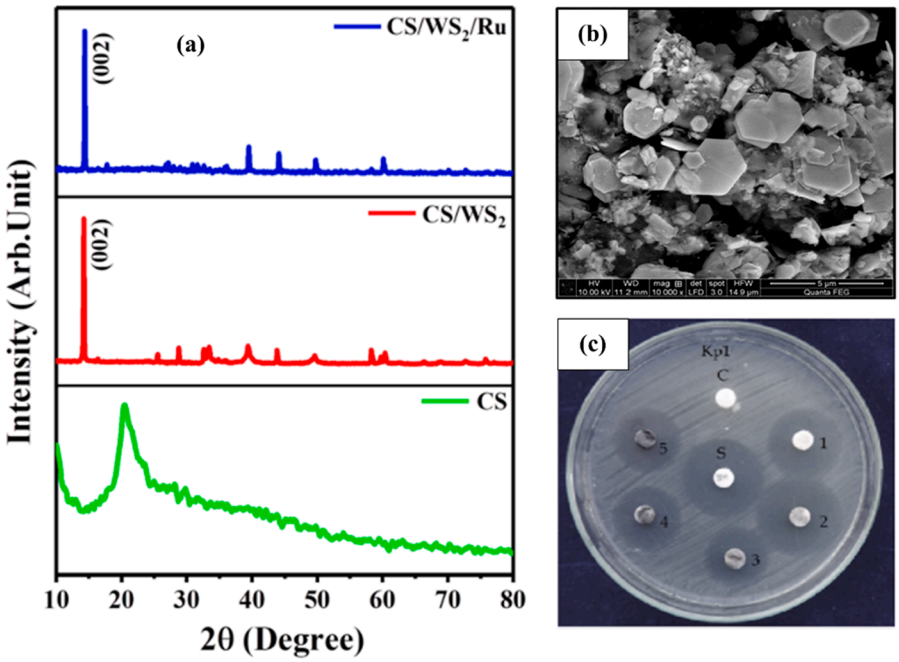

Figure 32. XRD spectra of all samples (**a**), SEM images of CS/WS_2/Ru composite (**b**), photographic representation of antibacterial activity of CS/WS_2/Ru against *E. coli* (**c**). Reproduced with permission [50]. Copyright 2021, Elsevier.

The recent research achieved on microorganisms' disinfection using WS_2-based nanomaterials is tabulated in Table 5.

Table 5. WS_2-based nanomaterials for microorganism' disinfection.

WS_2-Based Photocatalyst	Microorganism	Inactivation Performance	Ref.
WS_2 monolayer	*E. coli bacteria*	~99%, 120 min	[53]
Ag_2S@WS_2	*S. aureus*	99.93%, 20 min	[104]
	E. coli	99.84%, 20 min	
Graphene oxide/WS_2/Mg-doped ZnO	*S. aureus*, *E. coli*	Inhibition rings size: 6.07 and 8.64 mm, respectively	[105]
WS_2/Ag nanoparticles	*E. coli*	96%, 3 h	[106]
PMS/WS_2/Fe^{3+}	*E. coli*	97.3%, 1 min	[107]
CS/WS_2/Pd	*E. coli*	Zone of inhibition: 38 mm	[108]
	S. aureus	32 mm	
	B. subtilis	28 mm	
	K. pneumoniae	27 mm	
CS/WS_2/Ru	*E. coli*	Zone of inhibition: 37 mm	[50]
	S. aureus	31 mm	
	B. subtilis	29 mm	
	K. pneumoniae	27 mm	

4.3. Heavy Metals Reduction

Heavy metals are metals with high atomic weights, atomic numbers, and densities that are greater than 5 g/cm^3. The presence of heavy metals in water can cause poisoning of the living creatures, which leads to biodiversity damage, in addition to endangering human health when accumulating in the human body, causing cancers and organ failure. Examples of common heavy metals present in the environment are lead, cadmium, chromium, and arsenic [109,110]. Adopting strategies for the removal of heavy metal ions contaminating water is a great challenge for the scientific community currently. Some

convenient methods such as chemical precipitation and reverse osmosis are used. However, these techniques showed some restrictions and limitations, as they cannot achieve complete removal of the metal ions, as well as the formation of sludge in large amounts, which are difficult to be disposed of and managed properly [111–113]. Furthermore, photocatalysis can provide a continuous operation, as it does not need energy input except light energy. In addition, the photocatalytic redox reactions do not produce polluting intermediates, which makes it a green process for heavy metals reduction. Moreover, photocatalysis works on depositing heavy metals to be easily reduced on the surface of the photocatalyst as solids to be directly separated from the solution [114–117].

4.3.1. $CaIn_2S_4/WS_2$

Liu and his team fabricated a series of $CaIn_2S_4/WS_2$ (CW) hybrids through a simple hydrothermal method. WS_2 played a significant role as a cocatalyst that helped in increasing the visible light absorption, as well as the separation of charge carrier at the interface, which enhances the photocatalytic activity of the composite. The study concluded that the fabricated composite had a great performance in the photocatalytic reduction of Cr(VI), where the composite with 20wt% of WS_2 hybrid (Figure 33a) exhibited the highest Cr(VI) reduction rate of 98% as represented by Figure 33b. Moreover, the photogenerated electrons and O_2^- active radicals govern the photocatalytic Cr(VI).

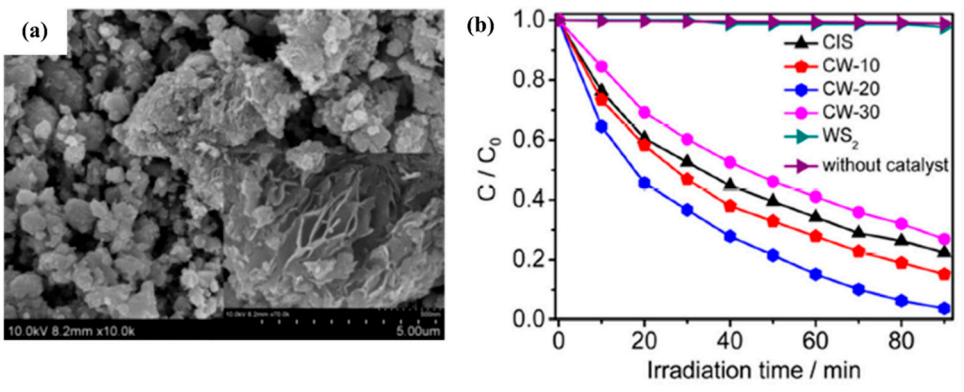

Figure 33. FE-SEM images of CW-20 (**a**), Cr(VI) reduction rates in the presence of the fabricated samples under visible light irradiation after 90 min (**b**). Reproduced with permission [118]. Copyright 2019, Elsevier.

4.3.2. $WS_2/BiOCl$

Ashraf, Bansal, Singh, and others prepared the novel hybrid nanosheet heterojunctions 2D/2D BiOCl/WS_2 (BW_x) through a simple and low-cost solution-based sonochemical route and studied its visible-light-driven photocatalytic response by comparing between the activity of BiOCl and BiOCl/WS_2 hybrid nanosheets on the photoreduction of Cr (VI) under visible light. The incident photon to electron conversion efficiency (IPCE) was used to estimate the quantum efficiency of the prepared samples. The study found that BiOCl/WS_2 (2%) (BW_2) exhibited the highest external quantum efficiency (EQE) in the UV and visible regions, and its FE-SEM image is shown in Figure 33a. This hybrid nanosheet photocatalyst achieved 94.9% of Cr(VI) removal efficiency (Figure 34b,c).

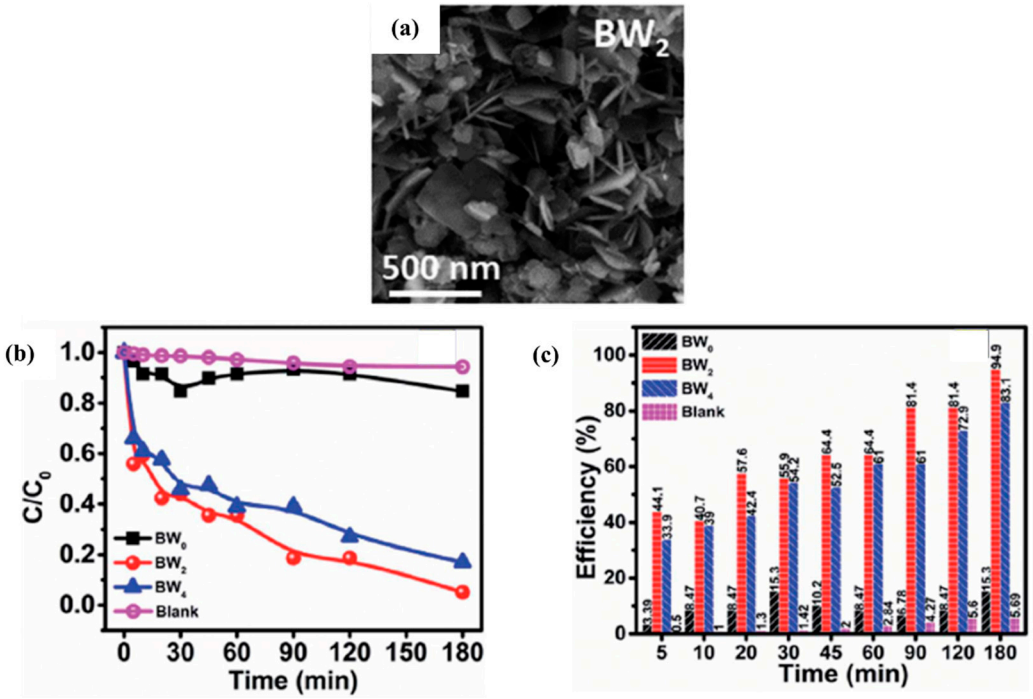

Figure 34. FE-SEM image of the as-prepared BW_2 hybrid nanosheets (**a**), Photocatalytic degradation of Cr (VI) without catalyst and in the presence of BW_0, BW_2, and BW_4 under visible light (**b**), Photocatalytic efficiency vs. time plot for Cr (VI) over BW_0, BW_2 and BW_4 hybrid nanosheets (**c**). Reproduced with permission [83]. Copyright 2020, Royal Chemical Society.

Overall, the researchers offered important insights into incorporating 2D TMDs in 2D BiOCl nanosheets to enhance bandgap engineering as well as to assist in the rate of charge transfer in order to increase the photocatalytic activity.

4.3.3. CdS/WS_2

Wang, Dou, Cao, and others designed a Z-scheme CdS/WS_2 (CW) heterojunction using a simple and green hydrothermal route. The heterojunction is composed of WS_2 nanosheets and CdS nanoparticles and it showed an excellent photoreduction for Cr (VI). The study used different molar ratios of CdS and WS_2 to tune the energy band structure of the composite, which helped in enhancing the separation efficiency and reducing the recombination of the photogenerated charge carriers. Figure 35a–f represent the morphologies of a bare CdS, WS_2, and CW-30 composite, which appears as CdS as nanoparticles attached on the surface of stacking structures of WS_2. The best photocatalytic activity was achieved by composite with 30% WS_2 with a reduction rate of 0.0846 per minute as concluded from Figure 35g,h. The fabricated heterojunction maintained high stability for four cycles of photocatalytic reduction of Cr (VI). This work provided an outstanding methodology to construct a Z-scheme WS_2-based heterojunction and then succeeded in implementing it in Cr(VI) photoreduction.

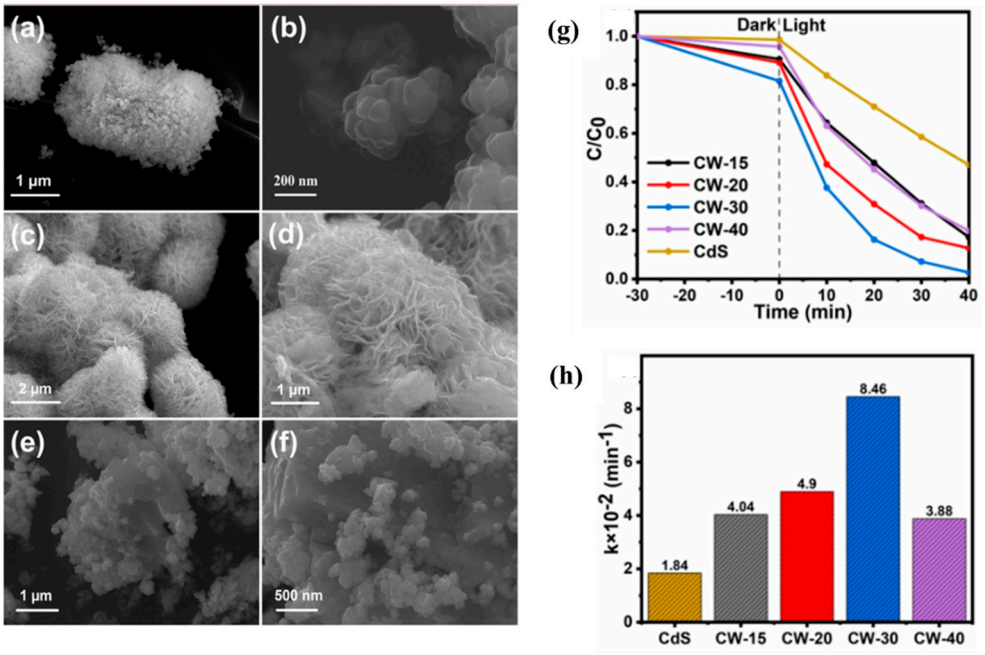

Figure 35. SEM images of bare CdS (**a**,**b**), bare WS_2 (**c**,**d**), and the CW-30 heterojunction (**e**,**f**), photocatalytic activity of the samples against Cr(IV) (**g**,**h**). Reproduced with permission [119]. Copyright 2022, Elsevier.

Table 6 summarizes the recent work on heavy metals reduction using WS_2-based nanomaterials.

Table 6. WS_2-based nanomaterials for heavy metals reduction.

WS_2-Based Photocatalyst	Metal Ion	Removal Efficiency	Ref.
$CaIn_2S_4/WS_2$	Cr (VI)	98%	[118]
WS_2/BiOCl	Cr (VI)	94.9%	[83]
CdS/WS_2	Cr (VI)	Reduction rate of 0.0846/min	[119]

4.4. Pharmaceuticals Photodegradation

Pharmaceutical waste is one of the most serious existing pollutants in water worldwide. There are several ways by which these pollutants were introduced to the environment such as hospital and domestic sewage, industrial discharge, and wastewater treatment plants. Pharmaceuticals are among the most significant contaminants of water, as they play a role in the alteration of the metabolic activity of the existing biota and hence can produce noticeable biochemical modifications. Currently, the world witnesses an extensive consumption of antibiotics, which caused an enormous increase in antibiotic wastes, and hence led to generating resistant bacteria, which threatens human health severely [120–122].

4.4.1. WS_2 Nanosheets

Fatima, Husian, Narang, and others performed a photocatalytic degradation of the antibiotic nitrofurantoin (NFT) by implementing novel WS_2 nanosheets that were fabricated using facile hydrothermal technique. The morphology of the nanosheets was studied using FE-SEM and HR-TEM as represented by Figure 36a,b. The fabricated WS_2 nanosheets showed excellent photocatalytic activity against NFT by degrading 90% of it in 120 min as concluded from the plot in Figure 36c.

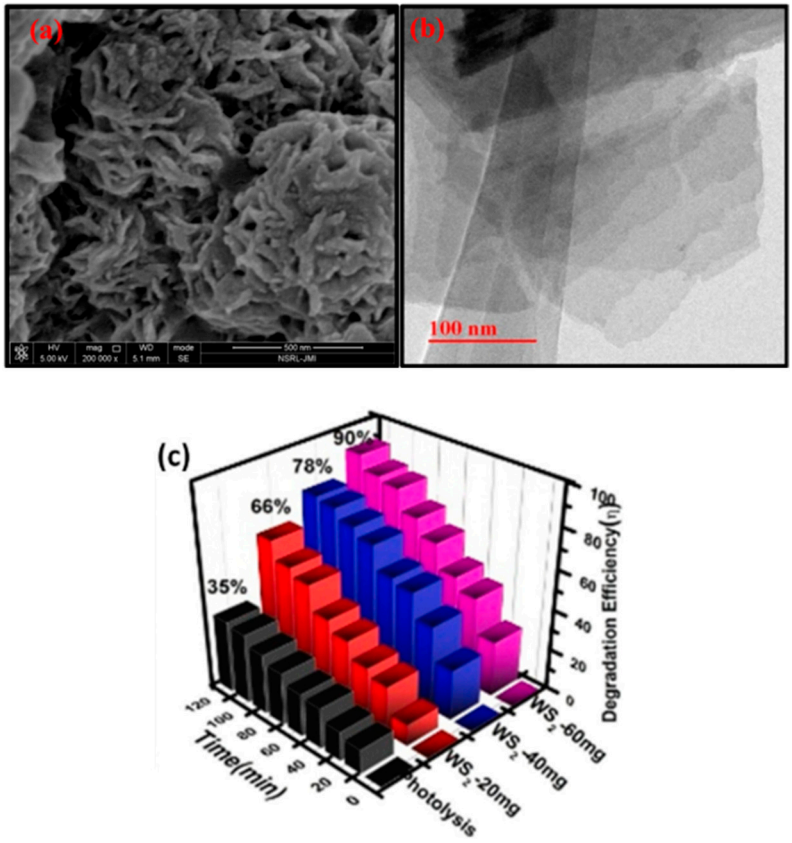

Figure 36. Images of as-prepared WS_2 nanosheets; FE-SEM (**a**), and HR-TEM (**b**), degradation efficiency over time for blank and fabricated samples (**c**). Reproduced with permission [44]. Copyright 2022, Elsevier.

4.4.2. Ag@Ag_2S/WS_2 and Ag@Ag_2O/WS_2

Torad, Mohamed, Khalil, and Ismail constructed WS_2 nanoplates modified with Ag_2S (~25–35 nm; Ag_2S/WS_2) and with Ag_2O (~10nm, Ag_2O/WS_2) through a deposition and then a hydrothermal approach to create innovative p-n heterojunction photocatalysts. They then used them to degrade diclofenac (DCF). The TEM image and the inset SAED in Figure 37a indicate that the monoclinic Ag_2S nanorods are well deposited on the surface of WS_2 nanoplates. It can be seen in Figure 37b that Ag_2O/WS_2 and Ag_2S/WS_2 achieved 80% and 92% of photodegradation of DCF, respectively. The authors stated that the fabricated Ag_2S/WS_2 showed an excellent photocatalytic degradation of diclofenac through H_2O_2 under visible light irradiation with a rate constant of 43.6×10^{-3} min^{-1}, which is higher than that of Ag_2O/WS_2. The improved photocatalytic performance of Ag_2S/WS_2 is due to the strong coupling of WS_2 nanoplates with Ag_2S creating higher surface area and pore volume. Figure 37c shows the predicted degradation pathway of DCF by the prepared heterojunction, which was discovered by liquid chromatograph-mass spectrometer (LC-MS). This research provided a useful approach for a novel commercially available photocatalyst that is active under visible light and that can be used for water treatment applications. In addition, it proved that supporting Ag_2O and Ag_2S on WS_2 can make a good Fenton-like catalyst.

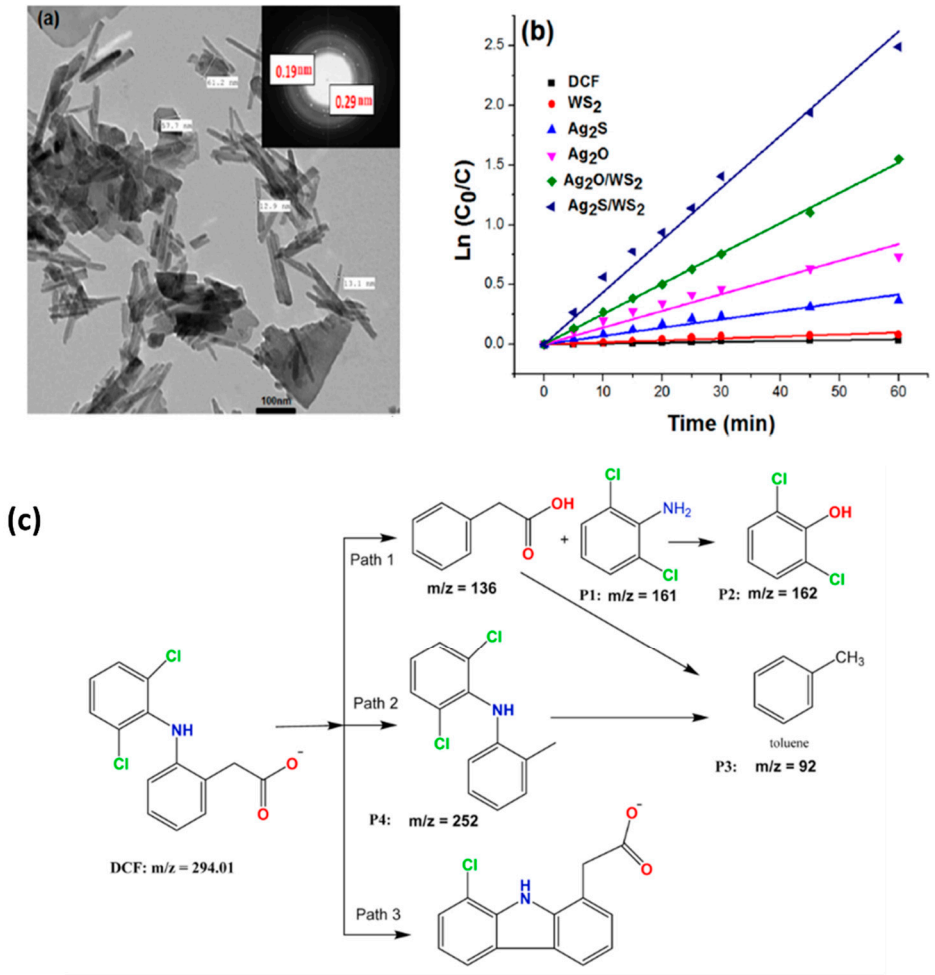

Figure 37. TEM image (inset is SAED image) of Ag_2S/WS_2 (**a**), ln (C_0/C) vs. irradiation time for the following reaction conditions: 0.006 g potassium diclofenac in 100 mL DW, 0.1 mL H_2O_2, 0.1 g catalyst, pH 12, and room temperature (**b**), the proposed pathways of DCF photodegradation using the prepared $Ag_2S@Ag@WS_2$ (**c**). Reproduced with permission [123]. Copyright 2021, Elsevier.

4.4.3. PMS/WS_2/Fe^{3+}

Luo, Liu, Cheng, and others integrated WS_2 in the system Fe/PMS (peroxymonosulfate) to increase the removal rate of carbamazepine (CBZ) and other water pollutants. The removal rate achieved by the modified heterojunction system was almost 100% in 10 min. This is due to the acceleration of the Fe^{3+}/Fe^{2+} cycle caused by WS_2 in addition to its participation in the activation of PMS. The authors compared the as-prepared six different systems in terms of their degradation effect and rate constants of CBZ degradation reaction as shown in Figure 38a and b, respectively. Moreover, the effect of WS_2 concentration was studied as seen in Figure 38c, which states that the degradation efficiency of CBZ increases with increasing the concentration of WS_2. Figure 38d and e represent SEM images of WS_2 before and after degradation. The authors used LC-MS to reveal the degradation pathway of CBZ based on its intermediates. Common anions were present in PMS/WS_2/Fe^{3+} systems such as HCO_3^- and Cl^- that had a significant inhibitory effect and promoting effect, respectively, on the degradation of CBZ.

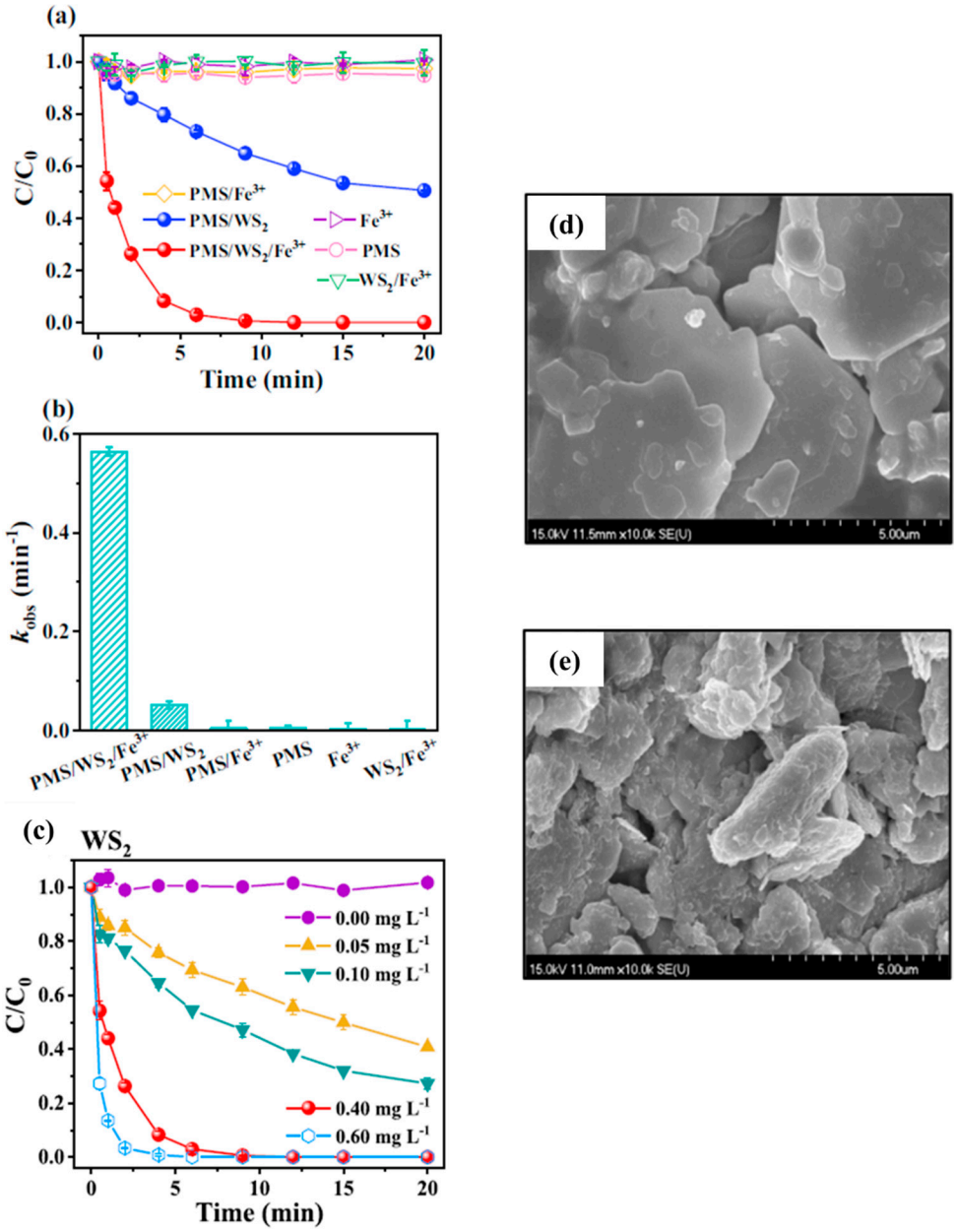

Figure 38. Time profiles of CBZ degradation in different systems at pH = 4.0 (**a**). Corresponding pseudo-first-order rate constants (**b**), Effects of concentrations of WS_2 in the degradation of CBZ in the system $PMS/WS_2/Fe^{3+}$ (**c**), SEM images of WS_2; before CBZ degradation (**d**), after degradation (**e**). Reproduced with permission [107]. Copyright 2021, Elsevier.

4.4.4. WS_2/BiOBr

Fu, Liu, Yan, and others succeeded in preparing a flower-like WS_2/BiOBr heterostructure with an ultrathin nanosheet via the one-pot hydrothermal method. The morphologies of the obtained microstructures were investigated using SEM as shown in Figure 39a–d, in addition to TEM and EDS. According to Figure 39e, WB-7 achieved the highest degradation efficiency of CIP among other WS_2 concentrations. However, WB-7 exhibited different photocatalytic degradation activity against the studied pharmaceuticals as shown in Figure 39f. This study reported an optimized heterojunction that showed an efficient photocatalytic activity and broad spectrum under visible-light irradiation for several water pollutants including popular pharmaceuticals such as ciprofloxacin (CIP), tetracycline (TC), metronidazole (MNZ), and oxytetracycline (OTC) varying in the following order: MNZ (97%) > TC (92%) > OTC (92%) > CIP (83%). The authors performed further

investigation of the photocatalytic process of CIP and concluded that the photocatalytic performance can be enhanced by meeting certain conditions including high CIP concentration, raised concentrations of ions (PO_4^{3-}, HPO_4^{2-}, $H_2PO_4^-$, and Cu^{2+}), and low pH values. The enhanced performance of the fabricated photocatalyst was linked to the ability of WS_2 to enhance light harvesting efficiency as well as to promote charge separation efficiency.

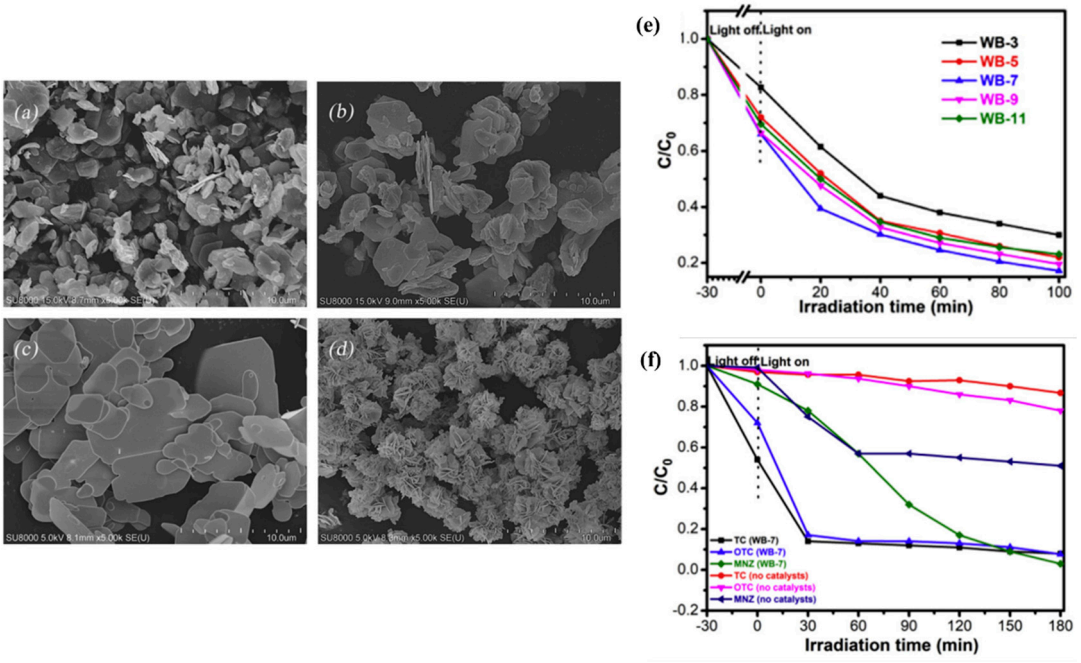

Figure 39. SEM images of WS_2-B (**a**), WS_2-N (**b**), pure BiOBr (**c**), and WB-7 (**d**), degradation efficiencies of CIP against WS_2/BiOBr with varying WS_2 concentration (**e**), photocatalytic degradation of TC, OTC, and MNZ in the presence of WB-7 (**f**). Reproduced with permission [124]. Copyright 2019, Elsevier.

4.4.5. g-C_3N_4/WS_2

The previously mentioned work above by Nawaz, Goudarzi, Saravanan, and Zarrin on the preparation of g-C_3N_4/WS_2 was also investigated toward tetracycline (TC). The fabricated heterostructure CNW-1.0 achieved 84.5% in 2 h. Figure 40a and b show the kinetics of TC photocatalytic degradation, the CNW-1.0 photocatalyst exhibited the highest kinetic rate constant, and it is higher than that of bare g-C_3N_4 with around 2.20 times. They proposed a photodegradation mechanism of the composite with TC and MB dye as follows:

$$\text{g-}C_3N_4/WS_2 + hv \text{ è g-}C_3N_4/WS_2 (e^-_{CB} + h^+_{VB}) \quad (7)$$

$$\text{g-}C_3N_4 (e^-_{CB}) + WS_2(h^+_{VB}) \text{ è g-}C_3N_4 + WS_2 \quad (8)$$

$$\text{g-}C_3N_4 (e^-_{CB}) + O_2 \text{ è} O_2^{\bullet -} \quad (9)$$

$$WS_2 (h^+_{VB}) + H_2O \text{ è } {}^{\bullet}OH \quad (10)$$

$$O_2^{\bullet -}, {}^{\bullet}OH + \text{TC and MB è degradation products} \quad (11)$$

$$\text{Degradation products} + (e^-/h^+) \text{ è } CO_2 + H_2O \quad (12)$$

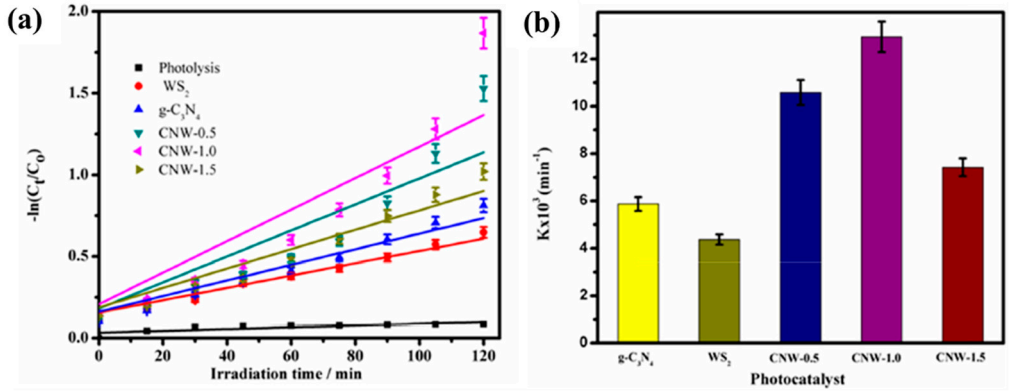

Figure 40. -ln(C_t/C_o) vs. irradiation time for each photocatalyst toward TC (**a**), the apparent first-order rate constant (k) of TC degradation via as-prepared samples (**b**). Reproduced with permission [20]. Copyright 2018, John Wiley and Sons.

Equations (7)–(12) demonstrate the significant role of charge transfer and charge carrier separation offered by the heterostructure prepared in the study for the degradation of both TC and MB. Electrons present in the CB of WS_2 are combined with the holes present in the VB of g-C_3N_4, which causes the accumulation of electron-hole pairs at the VB of WS_2 and the CB of g-C_3N_4. At the CB of g-C_3N_4, O_2^- radicals are produced by the reaction of electrons with the dissolved oxygen in the solution. Simultaneously, •OH radicals are produced at the VB of WS_2 by the reaction between holes and H_2O molecules. Consequently, the highly active photogenerated species contribute effectively to degrading MB and TC.

The work conducted on WS_2-based nanomaterials implemented in the photodegradation of pharmaceuticals is summarized in Table 7.

Table 7. WS_2-based nanomaterials for pharmaceuticals photodegradation.

WS_2-Based Photocatalyst	Pharmaceutical	Removal Efficiency	Ref.
WS_2 nanosheets	Nitrofurantoin (NFT)	90%, 120 min	[44]
Ag@Ag_2S/WS_2, Ag@Ag_2O/WS_2	Diclofenac (DCF)	92%, 80%, respectively	[123]
PMS/WS_2/Fe^{3+}	Carbamazepine (CBZ)	~100%, 10 min	[107]
WS_2/BiOBr	Ciprofloxacin (CIP)	83%	[124]
	Tetracycline (TC)	92%	
	Metronidazole (MNZ)	97%	
	Oxytetracycline (OTC)	92%	
g-C_3N_4/WS_2	Tetracycline (TC)	84.5%, 2 h	[20]

5. Conclusions

The investigation of the fundamentals of synthesis and applications of WS_2-nanostructured materials is still in continuous progress worldwide. The broad spectrum of applications in which WS_2 is employed has emerged from its superior properties as a TMD such as large specific surface area, tunable band gap, and high mobility. This review focused on the recent research work conducted on WS_2-based nanomaterials and their significant role in the photocatalytic water treatment process including the degradation of organic substances such as dyes and pesticides, disinfection of water, and killing pathogens, reduction of heavy metals, and degradation of drugs and pharmaceuticals. The mechanism by which photocatalysis degrades pollutants in water was also explained. In addition, the review highlighted the main techniques by which WS_2 nanostructures are synthesized such as hydrothermal, CVD, and LPE. It can be concluded that heterostructure construction is an essential solution to approach maximum degradation efficiency by reducing electron-hole pair separation and lowering the bandgap energy. Future research

should consider the need of sufficient understanding of the growth conditions and behaviors of WS_2. In addition, optimizing the operation parameters and developing new effective designs to enhance the performance of WS_2 for water treatment applications is urgently needed. In addition, new studies must focus on incorporating WS_2 nanostructures in a hybrid/composite photocatalyst to extend its advantages as a green and cost-effective system for water purification and environmental remediation.

Author Contributions: A.Y., writing and original draft preparation, review and editing; Z.T., review and editing; R.A.S., review and editing; T.A., conceptualization, comprehensive revision, and supervision. All authors have read and agreed to the published version of the manuscript.

Funding: Open Access funding provided by Qatar National Library.

Data Availability Statement: Data available in a publicly accessibility.

Conflicts of Interest: The authors declare no conflict of interest.

References

1. Jing, L.; Zhou, W.; Tian, G.; Fu, H. Surface tuning for oxide-based nanomaterials as efficient photocatalysts. *Chem. Soc. Rev.* **2013**, *42*, 9509–9549. https://doi.org/10.1039/C3CS60176E.
2. Alharbi, N.S.; Hu, B.; Hayat, T.; Rabah, S.O.; Alsaedi, A.; Zhuang, L.; Wang, X. Efficient elimination of environmental pollutants through sorption-reduction and photocatalytic degradation using nanomaterials. *Front. Chem. Sci. Eng.* **2020**, *14*, 1124–1135. https://doi.org/10.1007/s11705-020-1923-z.
3. Garg, A.; Singhania, T.; Singh, A.; Sharma, S.; Rani, S.; Neogy, A.; Wang, X. Photocatalytic Degradation of Bisphenol-A using N, Co Codoped TiO_2 Catalyst under Solar Light. *Sci. Rep.* **2019**, *9*, 765. https://doi.org/10.1038/s41598-018-38358-w.
4. Qutub, N.; Singh, P.; Sabir, S.; Sagadevan, S.; Oh, W.-C. Enhanced photocatalytic degradation of Acid Blue dye using CdS/TiO_2 nanocomposite. *Sci. Rep.* **2022**, *12*, 5759. https://doi.org/10.1038/s41598-022-09479-0.
5. Zhang, J.; Zhang, L.; Ma, X.; Ji, Z. A study of constructing heterojunction between two-dimensional transition metal sulfides (MoS_2 and WS_2) and (101), (001) faces of TiO_2. *Appl. Surf. Sci.* **2018**, *430*, 424–437. https://doi.org/10.1016/j.apsusc.2017.07.056.
6. Ahmad, R.; Ahmad, Z.; Khan, A.U.; Mastoi, N.R.; Aslam, M.; Kim, J. Photocatalytic systems as an advanced environmental remediation: Recent developments, limitations and new avenues for applications. *J. Environ. Chem. Eng.* **2016**, *4*, 4143–4164. https://doi.org/10.1016/j.jece.2016.09.009.
7. Li, S.; Wang, C.; Cai, M.; Yang, F.; Liu, Y.; Chen, J.; Zhang, P.; Li, X.; Chen, X. Facile fabrication of TaON/Bi_2MoO_6 core–shell S-scheme heterojunction nanofibers for boosting visible-light catalytic levofloxacin degradation and Cr(VI) reduction. *Chem. Eng. J.* **2022**, *428*, 131158. Available online: https://reader.elsevier.com/reader/sd/pii/S138589472102739X?token=D799FE216F506B28FC9A76E8F9EFC7EEA687C2DB4A2C5E4FC1B6619450B2316178BE5B5C01908DFCF9277A19062DAC7F&originRegion=eu-west-1&originCreation=20211216102211 (accessed on 16 December 2021).
8. Wang, W.; Zeng, Z.; Zeng, G.; Zhang, C.; Xiao, R.; Zhou, C.; Xiong, W.; Yang, Y.; Liu, Y.; Huang, D.; et al. Sulfur doped carbon quantum dots loaded hollow tubular g-C_3N_4 as novel photocatalyst for destruction of Escherichia coli and tetracycline degradation under visible light. *Chem. Eng. J.* **2019**, *378*, 122132. Available online: https://reader.elsevier.com/reader/sd/pii/S1385894719315268?token=E75BCF52D7CADB9C79C9153BB600C5717FE868F4BDB3A4177DF72392C836E5B307F44EBC39C8E62F8F3DF39E862C8B55&originRegion=eu-west-1&originCreation=20211216104206 (accessed on 16 December 2021).
9. Sahu, K.; Kuriakose, S.; Singh, J.; Satpati, B.; Mohapatra, S. Facile synthesis of ZnO nanoplates and nanoparticle aggregates for highly efficient photocatalytic degradation of organic dyes. *J. Phys. Chem. Solids* **2018**, *121*, 186–195. Available online: https://reader.elsevier.com/reader/sd/pii/S0022369717324393?token=5DC0699F806F4278530EE3223AEF547BF5347A5CAF0686D2B3FE4D7A973AA8408AC6906B379906548B22375646CF2A55&originRegion=eu-west-1&originCreation=20211216105136 (accessed on 16 December 2021).
10. George, R.; Bahadur, N.; Singh, N.; Singh, R.; Verma, A.; Shukla, A.K. Environmentally Benign TiO_2 Nanomaterials for Removal of Heavy Metal Ions with Interfering Ions Present in Tap Water. *Mater. Today Proc.* **2016**, *3*, 162–166.
11. Pelaez, M.; Nolan, N.T.; Pillai, S.C.; Seery, M.K.; Falaras, P.; Kontos, A.G.; Dunlop, P.S.M.; Hamilton, J.W.J.; Byrne, J.A.; O'Shea, K.; et al. A review on the visible light active titanium dioxide photocatalysts for environmental applications. *Appl. Catal. B Environ.* **2012**, *125*, 331–349.
12. Garg, A.; Basu, S.; Shetti, N.P.; Reddy, K.R. 2D materials and its heterostructured photocatalysts: Synthesis, properties, functionalization and applications in environmental remediation. *J. Environ. Chem. Eng.* **2021**, *9*, 106408. https://doi.org/10.1016/j.jece.2021.106408.
13. Wang, Y.; Xiao, X.; Lu, M.; Xiao, Y. 3D network-like rGO-$MoSe_2$ modified g-C_3N_4 nanosheets with Z-scheme heterojunction: Morphology control, heterojunction construct, and boosted photocatalytic performances. *J. Alloys Compd.* **2021**, *893*, 163197. https://doi.org/10.1016/j.jallcom.2021.163197.
14. Wang, Y.; Lei, S.; Zhang, X.; Zhou, S. First-principles study of nitrogen defect g-C_3N_4/WS_2 heterojunction on photocatalytic

activity. *Curr. Appl. Phys.* **2022**, *39*, 70–76. https://doi.org/10.1016/j.cap.2022.04.004.
15. Choi, W.; Choudhary, N.; Han, G.H.; Park, J.; Akinwande, D.; Lee, Y.H. Recent development of two-dimensional transition metal dichalcogenides and their applications. *Mater. Today* **2017**, *20*, 116–130.
16. Zhang, D.; Liu, T.; Cheng, J.; Liang, S.; Chai, J.; Yang, X.; Wang, H.; Zheng, G.; Cao, M. Controllable synthesis and characterization of tungsten disulfide nanosheets as promising nanomaterials for electronic devices. *Ceram. Int.* **2019**, *45*, 12443–12448. https://doi.org/10.1016/j.ceramint.2019.03.177.
17. Shalaby, M.S.; Sołowski, G.; Abbas, W. Recent Aspects in Membrane Separation for Oil/Water Emulsion. *Adv. Mater. Interfaces* **2021**, *8*, 2100448.
18. Zhang, N.; Yang, X.; Wang, Y.; Qi, Y.; Zhang, Y.; Luo, J.; Cui, P.; Jiang, W. A review on oil/water emulsion separation membrane material. *J. Environ. Chem. Eng.* **2022**, *10*, 107257. https://doi.org/10.1016/j.jece.2022.107257.
19. Mishra, A.K.; Lakshmi, K.V.; Huang, L. Eco-friendly synthesis of metal dichalcogenides nanosheets and their environmental remediation potential driven by visible light. *Sci. Rep.* **2015**, *5*, 15718.
20. Nawaz, A.; Goudarzi, S.; Saravanan, P.; Zarrin, H. Z-scheme induced g-C_3N_4/WS_2 heterojunction photocatalyst with improved electron mobility for enhanced solar photocatalysis. *Sol. Energy.* **2021**, *228*, 53–67. https://doi.org/10.1016/j.solener.2021.09.040.
21. Ma, S.; Zeng, L.; Tao, L.; Tang, C.Y.; Yuan, H.; Long, H.; Cheng, P.K.; Chai, Y.; Chen, C.; Fung, K.H.; et al. Enhanced Photocatalytic Activity of WS_2 Film by Laser Drilling to Produce Porous WS_2/WO_3 Heterostructure Methods and mechanisms for improvement of photocatalytic activity, are important and popular research topics for renewable energy production and waste water treatment OPEN. *Sci. Rep.* **2017**, *7*, 3125. Available online: www.nature.com/scientificreports/ (accessed on 1 June 2022).
22. Hazarika, S.J.; Mohanta, D. Inorganic fullerene-type WS_2 nanoparticles: Processing, characterization and its photocatalytic performance on malachite green. *Appl. Phys. A* **2017**, *123*, 381.
23. Hamd, W.; Daher, E.A.; Tofa, T.S.; Dutta, J. Recent Advances in Photocatalytic Removal of Microplastics: Mechanisms, Kinetic Degradation, and Reactor Design. *Front. Mar. Sci.* **2022**, *9*, 885614.
24. Kozlova, E.A.; Parmon, V.N. Heterogeneous semiconductor photocatalysts for hydrogen production from aqueous solutions of electron donors. *Russ. Chem. Rev.* **2017**, *86*, 870–906. Available online: https://iopscience.iop.org/article/10.1070/RCR4739 (accessed on 20 August 2022).
25. Ohtani, B. Revisiting the fundamental physical chemistry in heterogeneous photocatalysis: Its thermodynamics and kinetics Physical Chemistry Chemical Physics. *R. Soc. Chem.* **2014**, *16*, 1788–1897. Available online: https://pubs.rsc.org/en/content/articlehtml/2014/cp/c3cp53653j (accessed on 20 August 2022).
26. Subhiksha, V.; Kokilavani, S.; Sudheer Khan, S. Recent advances in degradation of organic pollutant in aqueous solutions using bismuth based photocatalysts: A review. *Chemosphere* **2022**, *290*, 133228. https://doi.org/10.1016/j.chemosphere.2021.133228.
27. Adhikari, S.; Kim, D.H. Synthesis of Bi_2S_3/Bi_2WO_6 hierarchical microstructures for enhanced visible light driven photocatalytic degradation and photoelectrochemical sensing of ofloxacin. *Chem. Eng. J.* **2018**, *354*, 692–705.
28. Guo, Q.; Zhou, C.; Ma, Z.; Yang, X. Fundamentals of TiO_2 Photocatalysis: Concepts, Mechanisms, and Challenges Advanced Materials. *Adv. Mater.* **2019**, *31*, 1901997. Available online: https://onlinelibrary.wiley.com/doi/full/10.1002/adma.201901997 (accessed on 20 August 2022).
29. Li, K.; An, X.; Park, K.H.; Khraisheh, M.; Tang, J. A critical review of CO_2 photoconversion: Catalysts and reactors. *Catal. Today* **2014**, *224*, 3–12.
30. Al Jitan, S.; Palmisano, G.; Garlisi, C. Synthesis and surface modification of TiO_2-based photocatalysts for the conversion of CO_2 Catalysts. *Multidiscip. Digit. Publ. Inst.* **2020**, *10*, 227. Available online: https://www.mdpi.com/2073-4344/10/2/227/htm (accessed on 20 August 2022).
31. Shtyka, O.; Ciesielski, R.; Kedziora, A.; Maniukiewicz, W.; Dubkov, S.; Gromov, D.; Maniecki, T. Photocatalytic Reduction of CO_2 Over Me (Pt, Pd, Ni, Cu)/TiO_2 Catalysts. *Top. Catal.* **2020**, *63*, 113–120. Available online: https://link.springer.com/article/10.1007/s11244-020-01241-y (accessed on 21 August 2022).
32. Zou, H.; Yan, X.; Ren, J.; Wu, X.; Dai, Y.; Sha, D.; Pan, J.; Liu, J. Photocatalytic activity enhancement of modified g-C_3N_4 by ionothermal copolymerization. *J. Mater.* **2015**, *1*, 340–347.
33. Ismael, M. A review on graphitic carbon nitride (g-C_3N_4) based nanocomposites: Synthesis, categories, and their application in photocatalysis. *J. Alloys Compd.* **2020**, *846*, 156446.
34. Chen, S.; Pan, Y.; Wang, D.; Deng, H. Structural Stability and Electronic and Optical Properties of Bulk WS_2 from First-Principles Investigations. *J. Electron. Mater.* **2020**, *49*, 7363–7369. https://doi.org/10.1007/s11664-020-08475-2.
35. Lv, R.; Robinson, J.A.; Schaak, R.E.; Sun, D.; Sun, Y.; Mallouk, T.E.; Terrones, M. Transition metal dichalcogenides and beyond: Synthesis, properties, and applications of single- and few-layer nanosheets. *Acc. Chem. Res.* **2015**, *48*, 56–64. Available online: https://pubmed.ncbi.nlm.nih.gov/25490673/ (accessed on 9 May 2022).
36. Zeng, Z.; Yin, Z.; Huang, X.; Li, H.; He, Q.; Lu, G.; Boey, H.; Zhang, H. Single-layer semiconducting nanosheets: High-yield preparation and device fabrication. *Angew. Chem.* **2011**, *50*, 11093–11097. Available online: https://pubmed.ncbi.nlm.nih.gov/22021163/ (accessed on 9 May 2022).
37. Gutiérrez, H.R.; Perea-López, N.; Elías, A.L.; Berkdemir, A.; Wang, B.; Lv, R.; López-Urías, R.; Crespi, V.H.; Terrones, H.; Terrones, S. Extraordinary room-temperature photoluminescence in triangular WS_2 monolayers. *Nano. Lett.* **2013**, *13*, 3447–3454. Available online: https://eres.qnl.qa/login?url=https://search.ebscohost.com/login.aspx?direct=true&db=cmedm&AN=23194096&site=ehost-live (accessed on 9 May 2022).
38. Yun, W.S.; Han, S.W.; Hong, S.C.; Kim, I.G.; Lee, J.D. Thickness and strain effects on electronic structures of transition metal

dichalcogenides: 2H-MX_2 semiconductors (M = Mo, W; X = S, Se, Te). *Phys. Rev. B* **2012**, *85*, 33305. https://doi.org/10.1103/physrevb.85.033305.
39. Liu, L.; Kumar, S.B.; Ouyang, Y.; Guo, J. Performance Limits of Monolayer Transition Metal Dichalcogenide Transistors. *IEEE Trans. Electron. Devices* **2011**, *58*, 3042–3047.
40. Al-Hilli, A.A.; Evans, B.L. The preparation and properties of transition metal dichalcogenide single crystals. *J. Cryst. Growth* **1972**, *15*, 93–101.
41. Jin, Q.; Dai, X.; Song, J.; Pu, K.; Wu, X.; An, J.; Zhao, T. High photocatalytic performance of g-C_3N_4/WS_2 heterojunction from first principles. *Chem. Phys.* **2021**, *545*, 111141.
42. Bin Rafiq, M.K.S.; Amin, N.; Alharbi, H.F.; Luqman, M.; Ayob, A.; Alharthi, Y.S.; Alharthi, N.H.; Bais, B.; Akhtaruzzaman, M. WS2: A New Window Layer Material for Solar Cell Application. *Sci. Rep.* **2020**, *10*, 771.
43. Green, M.A. Thin-film solar cells: Review of materials, technologies and commercial status. *J. Mater. Sci. Mater. Electron.* **2007**, *18*, 15–9.
44. Fatima, T.; Husain, S.; Narang, J.; Khanuja, M.; Shetti, N.P.; Reddy, K.R. Novel tungsten disulfide (WS_2) nanosheets for photocatalytic degradation and electrochemical detection of pharmaceutical pollutants. *J. Water Process. Eng.* **2022**, *47*, 102717. https://doi.org/10.1016/j.jwpe.2022.102717.
45. Voiry, D.; Yamaguchi, H.; Li, J.; Silva, R.; Alves, D.C.B.; Fujita, T.; Chen, M.; Asefa, T.; Shenoy, V.B.; Eda, G.; et al. Enhanced catalytic activity in strained chemically exfoliated WS_2 nanosheets for hydrogen evolution. *Nat. Mater.* **2013**, *12*, 850–855.
46. Cao, S.; Liu, T.; Hussain, S.; Zeng, W.; Peng, X.; Pan, F. Hydrothermal synthesis of variety low dimensional WS_2 nanostructures. *Mater. Lett.* **2014**, *129*, 205–208. https://doi.org/10.1016/j.matlet.2014.05.013.
47. Vattikuti, S.V.P.; Byon, C.; Chitturi, V. Selective hydrothermally synthesis of hexagonal WS_2 platelets and their photocatalytic performance under visible light irradiation. *Superlattices Microstruct.* **2016**, *94*, 39–50. https://doi.org/10.1016/j.spmi.2016.03.042.
48. Joseph, A.; Aneesh, P.M. Efficient degradation of methylene blue: A comparative study using hydrothermally synthesised SnS_2, WS_2 and VS_2 nanostructures. *Mater. Res. Bull.* **2022**, *146*, 111623.
49. Liu, X.; Chen, X.; Wang, S.; Yan, L.; Yan, J.; Guo, H.; Yang, F.; Lin, J. Promoting the photocatalytic H_2 evolution activity of $CdLa_2S_4$ nanocrystalline using few-layered WS_2 nanosheet as a co-catalyst. *Int. J. Hydrogen Energy* **2022**, *47*, 2327–2337.
50. Kasinathan, K.; Marimuthu, K.; Murugesan, B.; Sathaiah, M.; Subramanian, P.; Sivakumar, P.; Swaminathan, U.; Subbiah, R. Fabrication of eco-friendly chitosan functionalized few-layered WS_2 nanocomposite implanted with ruthenium nanoparticles for in vitro antibacterial and anticancer activity: Synthesis, characterization, and pharmaceutical applications. *Int. J. Biol. Macromol.* **2021**, *190*, 520–532. https://doi.org/10.1016/j.ijbiomac.2021.08.153.
51. Ling, X.; Lee, Y.H.; Lin, Y.; Fang, W.; Yu, L.; Dresselhaus, M.S.; Kong, J. Role of the seeding promoter in MoS_2 growth by chemical vapor deposition. *Nano. Lett.* **2014**, *14*, 464–472.
52. Mzerd, A.; Sayah, D.; Tedenac, J.C.; Boyer, A. Optimal crystal growth conditions of thin films of Bi_2Te_3 semiconductors. *J. Cryst. Growth* **1994**, *140*, 365–369. https://doi.org/10.1016/0022-0248(94)90312-3.
53. Thakur, D.; Sharma, M.; Vaish, R.; Balakrishnan, V. WS_2Monolayer for Piezo-Phototronic Dye Degradation and Bacterial Disinfection. *ACS Appl. Nano Mater.* **2021**, *4*, 7879–7887.
54. Chen, F.; Xia, Y.; Lv, Q.; Mao, S.; Li, Y. Growth and Optoelectronic Properties of Large-Scale Bilayer WS_2Ribbons with Unusual Shapes via Chemical Vapor Deposition. *J. Phys. Chem. C* **2022**, *126*, 1099–1106.
55. Thakur, D.; Kumar, P.; Sabarigresan, M.; Ramadurai, R.; Balakrishnan, V. Layer number dependent optical and electrical properties of CVD grown two-dimensional anisotropic WS_2. *Surf. Interfaces* **2021**, *26*, 101308.
56. Meng, L.; Yu, Y.; Yan, W.; Li, H.; Zhao, Q.; Yan, X. Growth mechanism of two-dimensional WS_2 film under the modulation of liquid metal. *Phys. E Low-Dimens. Syst. Nanostruct.* **2021**, *134*, 114885.
57. Coleman, J.N.; Lotya, M.; O'Neill, A.; Bergin, S.D.; King, P.J.; Khan, U.; Young, K.; Gaucher, A.; De, S.; Smith, R.J.; et al. Two-dimensional nanosheets produced by liquid exfoliation of layered materials. *Science* **2011**, *331*, 568–571. https://doi.org/10.1126/science.1194975.
58. Smith, R.J.; King, P.J.; Lotya, M.; Wirtz, C.; Khan, U.; De, S.; O'Neill, A.; Duesberg, G.S.; Grunlan, J.C.; Moriarty, G.; et al. Large-scale exfoliation of inorganic layered compounds in aqueous surfactant solutions. *Adv. Mater.* **2011**, *23*, 3944–3948. Available online: https://onlinelibrary.wiley.com/doi/full/10.1002/adma.201102584 (accessed on 1 June 2022).
59. Mohan, V.B.; Lau K tak Hui, D.; Bhattacharyya, D. Graphene-based materials and their composites: A review on production, applications and product limitations. *Compos. Part B Eng.* **2018**, *142*, 200–220.
60. Bonaccorso, F.; Bartolotta, A.; Coleman, J.N.; Backes, C. 2D-Crystal-Based Functional Inks. *Adv. Mater.* **2016**, *28*, 6136–6166. Available online: https://onlinelibrary.wiley.com/doi/full/10.1002/adma.201506410 (accessed on 1 June 2022).
61. Bonaccorso, F.; Colombo, L.; Yu, G.; Stoller, M.; Tozzini, V.; Ferrari, A.C.; Ruoff, R.S.; Pellegrini, V. Graphene, related two-dimensional crystals, and hybrid systems for energy conversion and storage. *Science* **2015**, *347*, 6217. https://doi.org/10.1126/science.1246501.
62. Hu, G.; Kang, J.; Ng, L.W.T.; Zhu, X.; Howe, R.C.T.; Jones, C.G.; Hersam, M.C.; Hasan, T. Functional inks and printing of two-dimensional materials. *Chem. Soc. Rev.* **2018**, *47*, 3265–3300. Available online: https://pubs.rsc.org/en/content/articlehtml/2018/cs/c8cs00084k (accessed on 1 June 2022).
63. Ashfaq, M.; Talreja, N.; Chauhan, D.; Viswanathan, M.R. Synthesis of Cu-doped 2D-WS_2 nanosheet-based nano-antibiotic materials for inhibiting E. Coli and S. aureus bacterial strains. *New J. Chem.* **2022**, *46*, 5581–5587.
64. Esfandiari, M.; Kamaei, S.; Rajabali, M.; Mohajerzadeh, S. High-performance large-area WS_2-based transistors by a novel tin-

oxide assisted liquid-phase exfoliation: Doping adjustment by plasma treatment. *2D Mater*. **2021**, *8*, 025013.
65. Tayebi, M.; Masoumi, Z.; Lee, B.K. Ultrasonically prepared photocatalyst of W/WO3 nanoplates with WS_2 nanosheets as 2D material for improving photoelectrochemical water splitting. *Ultrason. Sonochem.* **2021**, *70*, 105339. Available online: https://doi.org/10.1016/j.ultsonch.2020.105339.
66. Ren, X.; Wang, B.; Huang, Z.; Qiao, H.; Duan, C.; Zhou, Y.; Zhong, J.; Wang, Z.; Qi, X. Flexible self-powered photoelectrochemical-type photodetector based on 2D WS_2-graphene heterojunction. *FlatChem* **2021**, *25*, 100215. https://doi.org/10.1016/j.flatc.2020.100215.
67. Zhu, D.; Zhou, Q. Action and mechanism of semiconductor photocatalysis on degradation of organic pollutants in water treatment: A review. *Environ. Nanotechnol. Monit. Manag.* **2019**, *12*, 100255. https://doi.org/10.1016/j.enmm.2019.100255.
68. Wang, H.; Zhang, L.; Chen, Z.; Hu, J.; Li, S.; Wang, Z.; Liu, J.; Wang, X. Semiconductor heterojunction photocatalysts: Design, construction, and photocatalytic performances. *Chem. Soc. Rev.* **2014**, *43*, 5234–5244. https://doi.org/10.1039/c4cs00126e.
69. Fan, Y.; Chen, G.; Li, D.; Li, F.; Luo, Y.; Meng, Q. Enhancement of photocatalytic H_2 evolution on hexagonal CdS by a simple calcination method under visible light irradiation. *Mater. Res. Bull.* **2011**, *46*, 2338–2341. https://doi.org/10.1016/j.materresbull.2011.08.040.
70. Zong, X.; Wu, G.; Yan, H.; Ma, G.; Shi, J.; Wen, F.; Wang, L.; Li, C. Photocatalytic H_2 evolution on MoS_2/Cd_5 catalysts under visible light irradiation. *J. Phys. Chem. C* **2010**, *114*, 1963–1968. https://doi.org/10.1021/jp904350e.
71. Es'haghzade, Z.; Pajootan, E.; Bahrami, H.; Arami, M. Facile synthesis of Fe_3O_4 nanoparticles via aqueous based electro chemical route for heterogeneous electro-Fenton removal of azo dyes. *J. Taiwan Inst. Chem. Eng.* **2017**, *71*, 91–105. https://doi.org/10.1016/j.jtice.2016.11.015.
72. Yao, L.; Zhang, L.; Wang, R.; Chou, S.; Dong, Z.L. A new integrated approach for dye removal from wastewater by polyoxometalates functionalized membranes. *J. Hazard. Mater.* **2016**, *301*, 462–470. https://doi.org/10.1016/J.JHAZMAT.2015.09.027.
73. Tekin, G.; Ersöz, G.; Atalay, S. Degradation of benzoic acid by advanced oxidation processes in the presence of Fe or Fe-TiO_2 loaded activated carbon derived from walnut shells: A comparative study. *J. Environ. Chem. Eng.* **2018**, *6*, 1745–1759. https://doi.org/10.1016/J.JECE.2018.01.067.
74. Akerdi, A.G.; Es'Haghzade, Z.; Bahrami, S.H.; Arami, M. Comparative study of GO and reduced GO coated graphite electrodes for decolorization of acidic and basic dyes from aqueous solutions through heterogeneous electro-Fenton process. *J. Environ. Chem. Eng.* **2017**, *5*, 2313–2324. https://doi.org/10.1016/J.JECE.2017.04.028.
75. Byrne, C.; Subramanian, G.; Pillai, S.C. Recent advances in photocatalysis for environmental applications. *J. Environ. Chem. Eng.* **2018**, *6*, 3531–3555. https://doi.org/10.1016/J.JECE.2017.07.080.
76. Akerdi, A.G.; Bahrami, S.H. Application of heterogeneous nano-semiconductors for photocatalytic advanced oxidation of organic compounds: A review. *J. Environ. Chem. Eng.* **2019**, *7*, 103283. https://doi.org/10.1016/j.jece.2019.103283.
77. Ashraf, W.; Fatima, T.; Srivastava, K.; Khanuja, M. Superior photocatalytic activity of tungsten disulfide nanostructures: Role of morphology and defects. *Appl. Nanosci.* **2019**, *9*, 1515–1529. https://doi.org/10.1007/s13204-019-00951-4.
78. Koyyada, G.; Prabhakar Vattikuti, S.V.; Shome, S.; Shim, J.; Chitturi, V.; Jung, J.H. Enhanced solar light-driven photocatalytic degradation of pollutants and hydrogen evolution over exfoliated hexagonal WS_2 platelets. *Mater. Res. Bull.* **2019**, *109*, 246–254. https://doi.org/10.1016/j.materresbull.2018.09.045.
79. Wu, S.C.; Cheng, P.; Han, J.J.; Chen, Y.; Yan, X.; Guo, X.J.; Lang, W.Z. Construction of two-dimensional Ag/WS_2 hybrid membranes with self-cleaning ability by photocatalysis for efficient water filtration. *J. Membr. Sci.* **2022**, *641*, 119865. https://doi.org/10.1016/j.memsci.2021.119865.
80. Wu, X.F.; Li, H.; Zhang, Y.; Zhang, J.R.; Su, J.Z.; Feng, Y.M.; Zhang, W.G.; Sun, L.S.; Sun, X.G. Synthesis of AgI/WS_2 hybrids as a novel photocatalyst with efficient degradation of rhodamine B. *Micro Nano Lett.* **2019**, *14*, 173–177. https://doi.org/10.1049/mnl.2018.5189.
81. Li, L.; Cai, J.; Yan, Y.; Zhao, F.; Zhou, J. Flower-like direct Z-scheme WS_2/$Bi_2O_2CO_3$ photocatalyst with enhanced photocatalytic activity. *J. Alloys Compd.* **2019**, *810*, 151872. https://doi.org/10.1016/j.jallcom.2019.151872.
82. Fu, S.; Yuan, W.; Liu, X.; Yan, Y.; Liu, H.; Li, L.; Zhao, F.; Zhou, J. A novel 0D/2D WS_2/BiOBr heterostructure with rich oxygen vacancies for enhanced broad-spectrum photocatalytic performance. *J. Colloid Interface Sci.* **2020**, *569*, 150–163. https://doi.org/10.1016/j.jcis.2020.02.077.
83. Ashraf, W.; Bansal, S.; Singh, V.; Barman, S.; Khanuja, M. BiOCl/WS_2hybrid nanosheet (2D/2D) heterojunctions for visible-light-driven photocatalytic degradation of organic/inorganic water pollutants. *RSC Adv.* **2020**, *10*, 25073–25088. https://doi.org/10.1039/d0ra02916e.
84. Qi, S.; Liu, X.; Ma, N.; Xu, H. Construction and photocatalytic properties of WS_2/BiOCl heterojunction. *J. Nanoparticle Res.* **2020**, 22, 357. https://doi.org/10.1007/s11051-020-05087-z.
85. Zhang, Q.; Tai, M.; Zhou, Y.; Zhou, Y.; Wei, Y.; Tan, C.; Wu, Z.; Li, J.; Lin, H. Enhanced Photocatalytic Property of γ-$CsPbI_3$ Perovskite Nanocrystals with WS_2. *ACS Sustain. Chem. Eng.* **2020**, *8*, 1219–1229. https://doi.org/10.1021/acssuschemeng.9b06451.
86. Tran, H.H.; Truong, D.H.; Truong, T.T.; Xuan Dieu Nguyen, T.; Jin, Y.S.; Kim, S.J.; Vo, V. A Facile Synthesis of WS_2/g-C_3N_4 Composites with Improved Photocatalytic Activity. *Bull. Korean Chem. Soc.* **2018**, *39*, 965–971. https://doi.org/10.1002/bkcs.11536.
87. Zeng, P.; Ji, X.; Su, Z.; Zhang, S. WS_2/g-C_3N_4 composite as an efficient heterojunction photocatalyst for biocatalyzed artificial photosynthesis. *RSC Adv.* **2018**, *8*, 20557–20567. https://doi.org/10.1039/c8ra02807a.
88. Merci, S.; Saljooqi, A.; Shamspur, T.; Mostafavi, A. Investigation of photocatalytic chlorpyrifos degradation by a new silica

mesoporous material immobilized by WS_2 and Fe_3O_4 nanoparticles: Application of response surface methodology. *Appl. Organomet. Chem.* **2020**, *34*, e5343. https://doi.org/10.1002/aoc.5343.
89. Zhao, Y.; Liu, J.; Zhang, X.; Wang, C.; Zhao, X.; Li, J.; Jin, H. Convenient Synthesis of WS_2-MoS_2 Heterostructures with Enhanced Photocatalytic Performance. *J. Phys. Chem. C* **2019**, *123*, 27363-27368. https://doi.org/10.1021/acs.jpcc.9b08101.
90. Luo, S.; Dong, S.; Lu, C.; Yu, C.; Ou, Y.; Luo, L.; Sun, J.; Sun, J. Rational and green synthesis of novel two-dimensional WS_2/MoS_2 heterojunction via direct exfoliation in ethanol-water targeting advanced visible-light-responsive photocatalytic performance. *J. Colloid Interface Sci.* **2018**, *513*, 389–399. https://doi.org/10.1016/j.jcis.2017.11.044.
91. Qi, S.; Liu, X.; Ma, N.; Xu, H. Construction and photocatalytic properties of WS_2/MoS_2/BiOCl heterojunction. *Chem. Phys. Lett.* **2021**, *763*, 138203. https://doi.org/10.1016/j.cplett.2020.138203.
92. Barakat, M.A.; Kumar, R.; Almeelbi, T.; Al-Mur, B.A.; Eniola, J.O. Sustainable visible light photocatalytic scavenging of the noxious organic pollutant using recyclable and reusable polyaniline coupled WO_3/WS_2 nanohybrid. *J. Clean. Prod.* **2022**, *330*, 129942. https://doi.org/10.1016/j.jclepro.2021.129942.
93. Yu, W.; Chen, X.; Mei, W.; Chen, C.; Tsang, Y. Photocatalytic and electrochemical performance of three-Dimensional reduced graphene Oxide/WS_2/Mg-doped ZnO composites. *Appl. Surf. Sci.* **2017**, *400*, 129–138. https://doi.org/10.1016/j.apsusc.2016.12.138.
94. Zhang, X.; Qiu, F.; Rong, X.; Xu, J.; Rong, J.; Zhang, T. Zinc oxide/graphene-like tungsten disulphide nanosheet photocatalysts: Synthesis and enhanced photocatalytic activity under visible-light irradiation. *Can. J. Chem. Eng.* **2018**, *96*, 1053–1061. https://doi.org/10.1002/cjce.23039.
95. Cho, E.C.; Chang-Jian, C.W.; Zheng, J.H.; Huang, J.H.; Lee, K.C.; Ho, B.C.; Hsiao, Y.S. Microwave-assisted synthesis of TiO_2/WS_2 heterojunctions with enhanced photocatalytic activity. *J. Taiwan Inst. Chem. Eng.* **2018**, *91*, 489–498. https://doi.org/10.1016/j.jtice.2018.05.025.
96. Wu, Y.; Liu, Z.; Li, Y.; Chen, J.; Zhu, X.; Na, P. WS_2 nanodots-modified TiO_2 nanotubes to enhance visible-light photocatalytic activity. *Mater. Lett.* **2019**, *240*, 47–50. https://doi.org/10.1016/j.matlet.2018.12.056.
97. Liao, Y.; Yao, Y.; Yu, Y.; Zeng, Y. Enhanced Antibacterial Activity of Curcumin by Combination With Metal Ions. *Colloids Interface Sci. Commun.* **2018**, *25*, 1–6. https://doi.org/10.1016/j.colcom.2018.04.009.
98. Schwarzenbach, R.P.; Egli, T.; Hofstetter, T.B.; Von Gunten, U.; Wehrli, B. Global water pollution and human health. *Annu. Rev. Environ. Resour.* **2010**, *35*, 109–136. https://doi.org/10.1146/annurev-environ-100809-125342.
99. Santosham, M.; Chandran, A.; Fitzwater, S.; Fischer-Walker, C.; Baqui, A.H.; Black, R. Progress and barriers for the control of diarrhoeal disease. *Lancet* **2010**, *376*, 63–67. https://doi.org/10.1016/S0140-6736(10)60356-X.
100. Staedel, C.; Darfeuille, F. MicroRNAs and bacterial infection. *Cell. Microbiol.* **2013**, *15*, 1496–1507. https://doi.org/10.1111/cmi.12159.
101. WHO. *Guidelines for Drinking-Water Quality*. World Health Organization: Geneva, Switzerland, 2011; Volume 216, pp. 303–304.
102. Rengifo-Herrera, J.A.; Mielczarski, E.; Mielczarski, J.; Castillo, N.C.; Kiwi, J.; Pulgarin, C. Escherichia coli inactivation by N, S co-doped commercial TiO_2 powders under UV and visible light. *Appl. Catal. B Environ.* **2008**, *84*, 448–456. https://doi.org/10.1016/j.apcatb.2008.04.030.
103. Rengifo-Herrera, J.A.; Pierzchała, K.; Sienkiewicz, A.; Forró, L.; Kiwi, J.; Pulgarin, C. Abatement of organics and Escherichia coli by N, S co-doped TiO_2 under UV and visible light. Implications of the formation of singlet oxygen (1O2) under visible light. *Appl. Catal. B Environ.* **2009**, *88*, 398–406. https://doi.org/10.1016/j.apcatb.2008.10.025.
104. Lin, Y.; Han, D.; Li, Y.; Tan, L.; Liu, X.; Cui, Z.; Yang, X.; Li, Z.; Liang, Y.; Zhu, S.; et al. Ag_2S@WS_2 Heterostructure for Rapid Bacteria-Killing Using Near-Infrared Light. *ACS Sustain. Chem. Eng.* **2019**, *7*, 14982–14990. https://doi.org/10.1021/acssuschemeng.9b03287.
105. Chen, C.; Yu, W.; Liu, T.; Cao, S.; Tsang, Y. Graphene oxide/WS_2/Mg-doped ZnO nanocomposites for solar-light catalytic and anti-bacterial applications. *Sol. Energy Mater. Sol. Cells* **2017**, *160*, 43–53. https://doi.org/10.1016/j.solmat.2016.10.020.
106. Kumar, P.; Kataria, S.; Roy, S.; Jaiswal, A.; Balakrishnan, V. Photocatalytic Water Disinfection of CVD Grown WS_2 Monolayer Decorated with Ag Nanoparticles. *ChemistrySelect* **2018**, *3*, 7648–7655. https://doi.org/10.1002/slct.201800997.
107. Luo, H.; Liu, C.; Cheng, Y.; Zeng, Y.; He, D.; Pan, X. Fe(III) greatly promotes peroxymonosulfate activation by WS_2 for efficient carbamazepine degradation and Escherichia coli disinfection. *Sci. Total Environ.* **2021**, *787*, 147724. https://doi.org/10.1016/j.scitotenv.2021.147724.
108. Kasinathan, K.; Marimuthu, K.; Murugesan, B.; Samayanan, S.; Cai, Y.; Rathinam, C. Facile synthesis of highly biologically active chitosan functionalized 2D WS_2 nanocomposite anchored with palladium nanoparticles for antibacterial and anticancer activity: In-vitro biomedical evaluation. *J. Mol. Liq.* **2021**, *335*, 116582. https://doi.org/10.1016/j.molliq.2021.116582.
109. Fu, F.; Wang, Q. Removal of heavy metal ions from wastewaters: A review. *J. Environ. Manag.* **2011**, *92*, 407–418. https://doi.org/10.1016/J.JENVMAN.2010.11.011.
110. Litter, M.I. Mechanisms of removal of heavy metals and arsenic from water by TiO_2-heterogeneous photocatalysis. *Pure Appl. Chem.* **2015**, *87*, 557–567. https://doi.org/10.1515/PAC-2014-0710/PDF.
111. Engates, K.E.; Shipley, H.J. Adsorption of Pb, Cd, Cu, Zn, and Ni to titanium dioxide nanoparticles: Effect of particle size, solid concentration, and exhaustion. *Environ. Sci. Pollut. Res.* **2011**, *18*, 386–395. https://doi.org/10.1007/S11356-010-0382-3/FIGURES/5.
112. Skubal, L.R.; Meshkov, N.K.; Rajh, T.; Thurnauer, M. Cadmium removal from water using thiolactic acid-modified titanium dioxide nanoparticles. *J. Photochem. Photobiol. A Chem.* **2002**, *148*, 393–397. https://doi.org/10.1016/S1010-6030(02)00069-2.
113. Regmi, P.; Garcia Moscoso, J.L.; Kumar, S.; Cao, X.; Mao, J.; Schafran, G. Removal of copper and cadmium from aqueous solution

using switchgrass biochar produced via hydrothermal carbonization process. *J. Environ. Manag.* **2012**, *109*, 61–69. https://doi.org/10.1016/J.JENVMAN.2012.04.047.
114. Gao, X.; Meng, X. Photocatalysis for heavy metal treatment: A review. *Processes* **2021**, *9*, 1729. https://doi.org/10.3390/pr9101729.
115. Meng, X.; Zhang, Z.; Li, X. Synergetic photoelectrocatalytic reactors for environmental remediation: A review. *J. Photochem. Photobiol. C Photochem. Rev.* **2015**, *24*, 83–101. https://doi.org/10.1016/j.jphotochemrev.2015.07.003.
116. Kubota, Y.; Watanabe, K.; Tsuda, O.; Taniguchi, T. Deep ultraviolet light-emitting hexagonal boron nitride synthesized at atmospheric pressure. *Science* **2007**, *317*, 932–934. https://doi.org/10.1126/science.1144216.
117. Xie, W.; Zhang, M.; Liu, D.; Lei, W.; Sun, L.; Wang, X. Photocatalytic TiO_2/porous BNNSs composites for simultaneous LR_2B and Cr (VI) removal in wool dyeing bath. *J. Photochem. Photobiol. A Chem.* **2017**, *333*, 165–173. https://doi.org/10.1016/j.jphotochem.2016.10.024.
118. Liu, B.; Liu, X.; Li, L.; Zhuge, Z.; Li, Y.; Li, C.; Gong, Y.; Niu, L.; Xu, S.; Sun, C.Q. $CaIn_2S_4$ decorated WS_2 hybrid for efficient Cr(VI) reduction. *Appl. Surf. Sci.* **2019**, *484*, 300–306. https://doi.org/10.1016/j.apsusc.2019.03.322.
119. Wang, G.; Dou, K.; Cao, H.; Du, R.; Liu, J.; Tsidaeva, N.; Wang, W. Designing Z-scheme CdS/WS_2 heterojunctions with enhanced photocatalytic degradation of organic dyes and photoreduction of Cr (VI): Experiments, DFT calculations and mechanism. *Sep. Purif. Technol.* **2022**, *291*, 120976. https://doi.org/10.1016/j.seppur.2022.120976.
120. Kumar, E.; Holt, W. V Impacts of Endocrine Disrupting Chemicals on Reproduction in Wildlife. In *Advances in Experimental Medicine and Biology*; Springer: New York, NY, USA, 2014; Volume 753, pp. 55–70.
121. Cesaro, A.; Belgiorno, V. Removal of Endocrine Disruptors from Urban Wastewater by Advanced Oxidation Processes (AOPs): A Review. Open Biotechnol. J. **2016**, 10, 151–172. https://doi.org/10.2174/1874070701610010151.
122. Petrie, B.; Barden, R.; Kasprzyk-Hordern, B. A review on emerging contaminants in wastewaters and the environment: Current knowledge, understudied areas and recommendations for future monitoring. *Water Res.* **2015**, *72*, 3–27. https://doi.org/10.1016/j.watres.2014.08.053.
123. Torad, E.; Mohamed, M.M.; Khalil, M.M.H.; Ismail, E.H. Optimal design of silver@silver sulfide-modified WS_2 and its application in photocatalytic diclofenac degradation and H_2 generation. *J. Environ. Chem. Eng.* **2021**, 9, 106446. https://doi.org/10.1016/j.jece.2021.106446.
124. Fu, S.; Liu, X.; Yan, Y.; Li, L.; Liu, H.; Zhao, F.; Zhou, J. Few-layer WS_2 modified BiOBr nanosheets with enhanced broad-spectrum photocatalytic activity towards various pollutants removal. *Sci. Total Environ.* **2019**, *694*, 133756. https://doi.org/10.1016/j.scitotenv.2019.133756.